OKANAGAN

Particle-in-Cell Modelling of Negative Ion Sources

Investigating the Negative Ion Production Discrepancy Between Hydrogen and Deuterium

Connor MacKenzie

A Directed Studies thesis submitted for credit toward the B.Sc. in Physics

University of British Columbia, Okanagan
Department of Physics

April 2025

Land Acknowledgement

This research was conducted on the unceded territory of the Syilx Okanagan Nation. For thousands of years, the Syilx people lived sustainably across this land, relying on their deep knowledge of local resources through hunting, fishing, growing, and trading.
Colonial settlement disrupted this way of life, dividing communities and dispossessing them from the land without a negotiated treaty—an injustice that remains unresolved. Despite this, the Syilx Okanagan Nation continues to affirm their connection to and stewardship of the territory.
I acknowledge this history with respect and gratitude, and recognize the responsibility that comes with working on these lands.

Project Title:

Particle-in-Cell Modelling of Negative Ion Sources with Vibrationally Resolved Cross-Section Handling

Academic Supervisors: Dr. Christina Haston, Dr. Gwenael Fubiani, Dr. Nicolas Savard
Industry Supervisor: Dr. Morgan Dehnel
Course Instructor / Examiner: Christina Haston

Abstract

This work investigates the computational modeling of plasma dynamics in ion sources using Particle-in-Cell (PIC) simulations. The goal is to understand discrepancies in negative ion-production observed in various ion sources when operating with hydrogen (H^-) and deuterium (D^-). To simulate the behavior of the D-PACE-TRIUMF liscenced RF-Powered Ion Source, the ITER BATMAN ion source was used as a proxy due to its similar geometry and RF-driven operation. Simulations were performed using a 2D PIC-MCC code developed by Dr. Gwenael Fubiani to model both plasma behavior and extraction dynamics.

In the first set of simulations, two seperate cases were conducted: one modeling H^- production and the other D^- production. The only difference between the two was a twofold increase in ion mass to approximate the difference between hydrogen and deuterium. Comparisons were made between ion flux, number density, and electric potential.

Motivated by these results, a second simulation was carried out under similar conditions, with one key modification: the magnetic force acting on negative ions was neglected. This adjustment aimed to isolate the effect of the magnetic field on the spatial density profiles of H^- and D^- ions.

To elevate this research to a publishable level, the implementation of an updated cross-section database became essential, as the standard dataset is outdated. The final phase of this PHYS 448 thesis focuses on the data science infrastructure required to integrate improved cross-section data provided by collaborators at CNR Bari, Italy.

The study concludes with the development of an automated Python-based framework for processing and formatting these cross-section datasets into structured input files for use in simulation workflows. A MITACS grant has been submitted to support a four-month internship under the academic supervision of Dr. Christina Haston, with industry guidance from D-PACE and Accel-Link Ltd lead by Dr. Morgan Dehnel(Selkirk Ion Source Research Chair). This internship will enable the continued implementation of the deuterium cross-section files into the PIC-MCC model, while also extending the automated framework to support updated hydrogen cross sections using the same infrastructure built during the deuterium data compilation. Together, the integration of updated cross-section data and the automated data-handling framework represents a critical step toward achieving more accurate and physically consistent plasma simulations. This advancement not only enhances the predictive power of simulation results but also strengthens their alignment with experimental measurements—ultimately contributing to more efficient ion source design and improved negative ion production.

Contents

Chapter 1

Introduction

1.1 Background: H-/D- Problem

The production of negative hydrogen (H^-) and deuterium (D^-) ions in volume-cusp ion sources is fundamental to a range of applications, from accelerator-based medical isotope production to particle physics research. However, there is a well-recognized challenge: D^- beam currents are consistently lower than those of H^-. For medical cyclotron operators who depend on high-intensity D^- beams for the efficient production of radioisotopes, this difference is a significant constraint.

For example, D-Pace's TRIUMF-licensed volume-cusp ion source produces 15 mA of H^- compared to only 5 mA of D^- [9], yielding a ratio of approximately 3:1. This trend is also seen in other commercial cyclotrons: the IBA C30XP generates 350 μA of H^- versus 100 μA of D^- (3.5:1) [11], while the ACSI TR19/9 produces 400 μA of H^- and 75 μA of D^- (5.3:1) [11]. Similarly, the ACSI TR30/15 [8] and SHI MP-30 [11] cyclotrons display ratios of 3.3:1 and 4:1, respectively. These consistent differences highlight the ongoing challenge of enhancing D^- production relative to H^-, which is critical for improving radioisotope production efficiency.

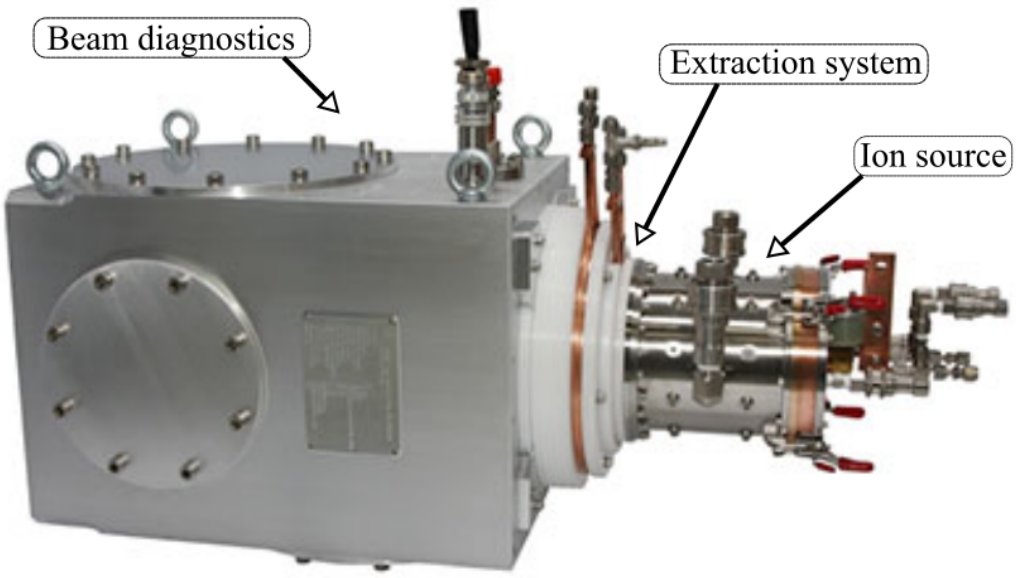

Figure 1.1: Overview of the D-Pace TRIUMF-licensed RF-powered ion source setup. [7]

Efforts to improve D^- beam output from volume-cusp ion sources have so far achieved only limited

success. Experimental work by D-Pace [7] and others has led to small, incremental gains, but a comprehensive theoretical or computational approach to systematically address the H^-/D^- disparity remains lacking. Most of the existing research focuses on experimental diagnostics, and there is a noticeable gap in comparative numerical studies that directly analyze H^- and D^- plasmas within the same ion source configuration. While particle-in-cell (PIC) simulations have been carried out for each species individually [14, 5, 6], no studies have been found that compare H^- and D^- under identical simulated conditions.

This thesis aims to contribute to a deeper understanding of the H^-/D^- production imbalance through numerical simulations and theoretical modeling of volume-cusp ion sources. In particular, the ITER BATMAN ion source is used as a model system, serving as a proxy for the TRIUMF D-Pace volume-cusp source due to its similar RF-driven design.

1.2 Plasma Generation

In volume-cusp ion sources, plasma is generated by a RF antenna that produces an alternating electric field, inducing a current which ionizes the neutral gas within the discharge region [9]. This ionization occurs inside the inductively coupled plasma (ICP) chamber, after which the plasma expands into an adjacent region known as the expansion chamber [1]. This configuration—featuring an expansion chamber positioned downstream of the RF discharge—is referred to as a "tandem" ion source.

A magnetic field is applied in the expansion chamber, oriented perpendicular to the electron flux (Γ_e) emerging from the ICP. Positioned at the far end of this chamber is the plasma grid (PG), which separates the ion source from the extraction and acceleration region. The PG plays a key role in suppressing electron leakage, thereby reducing the number of co-extracted electrons.

The applied magnetic field limits electron mobility in the axial direction, increasing the likelihood of collisions and promoting energy losses that reduce the local gas temperature. Electrons diffusing from the discharge interact with the magnetic field and are redirected toward the lateral walls of the source via the Lorentz force. Transport toward the PG occurs primarily through collisions and $E \times B$ drifts, with the effective electron displacement determined by the Larmor radius [4]. Figure 1.2 shows a cross-section of the ITER-BATMAN ion source.

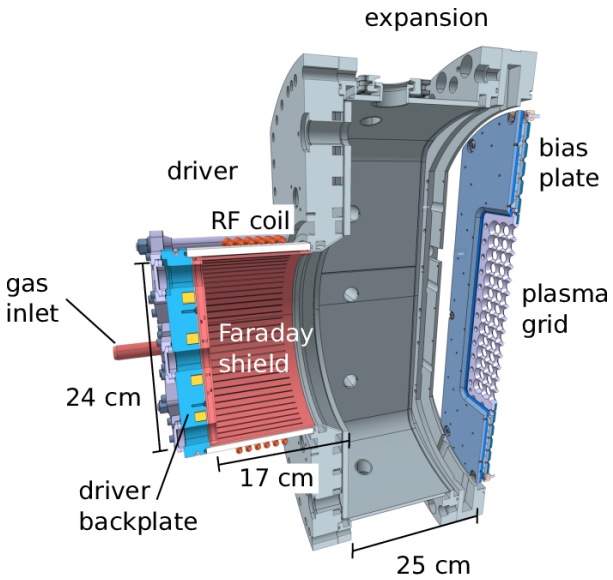

Figure 1.2: Schematic representation of the BATMAN prototype ion source at the Max Planck Institute, Garching, Germany.

To understand and predict the behavior of plasmas generated in ion souces such as ITER BATMAN, it is useful to go beyond a macroscopic or qualitative approach. The plasmas evolution within the source is a result of collective interactions between vast numbers of charged particles which are influenced by electromagnetic fields. These dynamics are inherently kinetic in nature. To capture this

complexity, we begin with a principle approach by considering a microscopic description of individual particle motion – the N-body problem. From there we build toward the kinetic and fluid equations that underpin modern plasma simulation methods, including the Vlasov equation (1.1).

1.3 Kinetic Description of a Plasma

To model the dynamics of a plasma, we begin by considering the statistical behavior of a large number of charged particles interacting through electromagnetic forces [4]. Rather than tracking each particle individually, we describe the system using a distribution function $f(\mathbf{x}, \mathbf{v}, t)$, which represents the number density of particles in phase space.

In the collisionless limit—appropriate for many low-density plasmas where particle collisions are rare—the evolution of this distribution is governed by the *Vlasov equation*:

$$\frac{\partial f}{\partial t} + \mathbf{v} \cdot \nabla_{\mathbf{x}} f + \frac{q}{m} (\mathbf{E} + \mathbf{v} \times \mathbf{B}) \cdot \nabla_{\mathbf{v}} f = 0. \tag{1.1}$$

This equation describes how the distribution function evolves due to the motion of particles through space and their acceleration by electromagnetic fields. The electric and magnetic fields, in turn, are governed by Maxwell's equations, which must be solved self-consistently with the Vlasov equation. Together, these form the foundation of kinetic plasma theory. The PIC algorithm is driven by the space and time discretization of the vlasov equation as demonstrate in [1].

A complete derivation of the Vlasov equation—starting from the N-body problem and progressing through the Klimontovich and kinetic equations—is provided in Appendix A.

1.4 Numerical Model

The simulation employs a Particle-In-Cell algorithm with Monte-Carlo-Collisons (PIC-MCC). This model is an explicit algorithm where particle trajectories are calculated based on field calculations of a previous time step [1]. With the computational domain discretized to a form 2D grid, by sequential time step, particle positions are used to compute species number density. As an initial condition, the simulation grid begins with an initial species specific number density N_i. Number density provides an analogous charge density to compute the plasma potential:

$$\nabla^2 \phi = -\frac{\rho}{\epsilon_0}$$

Now that we have an electric potential, ϕ we can compute the electric field.

$$\vec{E} = -\nabla \phi$$

With an electric field the velocities can be updated via the lorentz equation:

$$\vec{F} = q(\vec{E} + \vec{v} \times \vec{B}) \tag{1.2}$$

The updated velocity pushes our particles to their next positions. This process is repeated until the plasma paramaters reach a saturation and remain constant. Figure 1.3 is a visual shematic of the PIC algorithm.

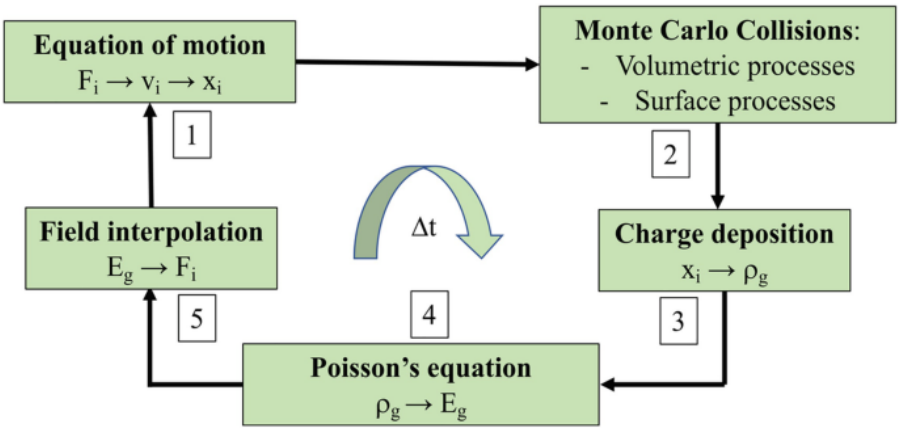

Figure 1.3: PIC/MCC algorithm visualization [1]

Scaling

To ensure accurate and numerically stable simulations, the choice of time step and spatial grid resolution is guided by fundamental plasma parameters [1]:

- The time step, Δt, is selected as a fraction of the electron plasma period, which represents the natural oscillation frequency of electrons. This ensures that the fastest electron-scale dynamics are properly resolved.
- The spatial grid size, Δx, is chosen to be on the order of the electron Debye length, which characterizes the screening effect of charges in a plasma. This choice captures key plasma physics phenomena while preventing artificial numerical effects.

The Debye length, λ_D, is defined as:

$$\lambda_D = \sqrt{\frac{\varepsilon_0 k_B T}{n_e e^2}} \tag{1.3}$$

where:

- λ_D: Debye length (m),
- ε_0: Permittivity of free space ($\varepsilon_0 \approx 8.85 \times 10^{-12}\,\mathrm{F/m}$),
- k_B: Boltzmann constant ($k_B \approx 1.38 \times 10^{-23}\,\mathrm{J/K}$),
- T: Electron temperature (K),
- n_e: Electron number density (m^{-3}),
- e: Elementary charge ($e \approx 1.60 \times 10^{-19}\,\mathrm{C}$).

Setting $\Delta t \ll \omega_{pe}^{-1}$, where ω_{pe} is the electron plasma frequency, and ensuring $\Delta x \approx \lambda_D$ are crucial for resolving charge separation effects and maintaining numerical stability in particle-in-cell (PIC) and fluid simulations.

Negative ion sources present a unique computational challenge due to their high plasma densities and large physical dimensions. The system size often spans tens of centimeters, while critical small-scale structures, such as the Debye length, are only on the order of tens of micrometers. This results in a vast disparity in length scales, which makes direct full-scale multi-dimensional simulations computationally prohibitive. A straightforward approach using fine grids and small time steps would require an impractically large number of grid points and particles, exceeding current computational capabilities.

To address these challenges, scaling techniques are employed. Instead of simulating the full system at physical plasma densities and device dimensions, a scaled-down version is used, where certain

parameters are adjusted to reduce computational requirements while preserving key plasma behaviors. One common approach involves modifying the vacuum permittivity, ε_0, or artificially increasing the Debye length by lowering the plasma density. This method allows for meaningful physical insights while ensuring that the fundamental physics of the system remains consistent.

By leveraging these scaling strategies, simulations can capture essential plasma dynamics with manageable computational resources, enabling better predictions and optimizations for real-world negative ion sources.

Simulating Power Absorption

The RF power absorption in hydrogen or deuterium plasma, as induced by the inductively coupled coil, is not directly simulated. Instead, a predefined absorbed power per time step is assumed. Due to their low mass, electrons primarily absorb this energy and redistribute it throughout the plasma via modeled elastic and inelastic collisions. Electrons undergoing heating collisions are assigned new velocities sampled from a Maxwellian distribution with a temperature calculated from the average electron energy and the absorbed energy per colliding particle. The electron heating mechanism follows an energy balance equation:

$$\frac{3}{2}T_h = \langle E_k \rangle_h + \frac{P_{\text{abs}}}{eN_e\nu_h} \tag{1.4}$$

where T_h is the heating temperature, $\langle E_k \rangle_h$ is the average electron kinetic energy, P_{abs} is the absorbed RF power, N_e is the electron number density, ν_h is the heating collision frequency, and e is the elementary charge.

ITER-type tandem sources operate with inductively coupled plasma (ICP) discharges that couple high RF power (typically $\sim$ 100 kW at $\sim$ 1 MHz) to a hydrogen or deuterium plasma. Instead of explicitly simulating the RF-plasma interaction, macroparticles within the power deposition region are stochastically heated based on an artificial heating collision frequency. The number of electrons experiencing heating collisions per time step is given by:

$$N_{\text{colliding}} = N_{\text{em}}\nu_h\Delta t \tag{1.5}$$

where N_{em} is the total number of macroparticles in the heating region. These electrons undergo velocity reassignment based on a Maxwellian distribution at the computed heating temperature.

The simulated electron temperature profile remains approximately uniform within the discharge, consistent with experimental observations in low-pressure, low-RF-frequency ($\sim$ 1 MHz) discharges. In these conditions, electron thermal velocity is high ($T_e \sim 10$ eV), and the mean free path is comparable to the discharge radius, allowing energy to be efficiently redistributed. A self-consistent RF energy coupling model would be required for precise distribution estimations; however, a practical approach is to impose experimentally observed non-Maxwellian EEDFs and study their influence on plasma properties [1].

1.5 Plasma Asymmetry

In the ITER-BATMAN ion source, experimental observations show that electron drift toward the lateral walls of the expansion chamber leads to charge separation, which generates a transverse electric field. This configuration is analogous to the Hall effect in semiconductors, where a magnetic field applied perpendicular to a current causes charge buildup on opposing sides, establishing a measurable transverse voltage.

In the expansion region, the applied magnetic field is typically oriented out of the ion drift plane ($\vec{B} = B_0\hat{z}$), while an ambipolar electric field develops radially across the chamber ($\vec{E} = E_x\hat{x}$). Under these conditions, electrons experience a net drift due to the combined effects of the electric field, pressure gradients, and Lorentz force, resulting in a component of electron flux transverse to both $\vec{E}$ and $\vec{B}$.

The electron flux $\vec{\Gamma}_e$ under these conditions can be expressed as [1]:

$$\vec{\Gamma}_e = \frac{1}{1+\Omega^2}\left(\vec{G} - \vec{G}\times\vec{\Omega} + (\vec{\Omega}\cdot\vec{G})\vec{\Omega}\right), \tag{1.6}$$

where $\vec{G} = -\mu_e(\nabla P_e + n_e e\vec{E})$ is the generalized driving force on the electrons, and $\vec{\Omega} = \mu_e\vec{B}$ is the normalized magnetic field vector (mobility-weighted).

To illustrate this, we consider a simplified configuration:

- Magnetic field: $\vec{B} = B_z(x)\hat{z}$
- Electric field: $\vec{E} = E_x\hat{x}$
- Approximate driving term: $\vec{G} \approx -n_e e\mu_e E_x\hat{x}$

Then the dominant drift term becomes:

$$\vec{G}\times\vec{\Omega} \propto (-\hat{x})\times(\hat{z}) = +\hat{y},$$

indicating a transverse electron drift in the $+\hat{y}$ direction—perpendicular to both the electric and magnetic fields. This drift displaces electrons toward one side of the chamber, where they may be lost to the wall or recombine with ions. The resulting charge separation modifies the plasma potential and contributes to spatial asymmetries in the transport and distribution of H^- ions.

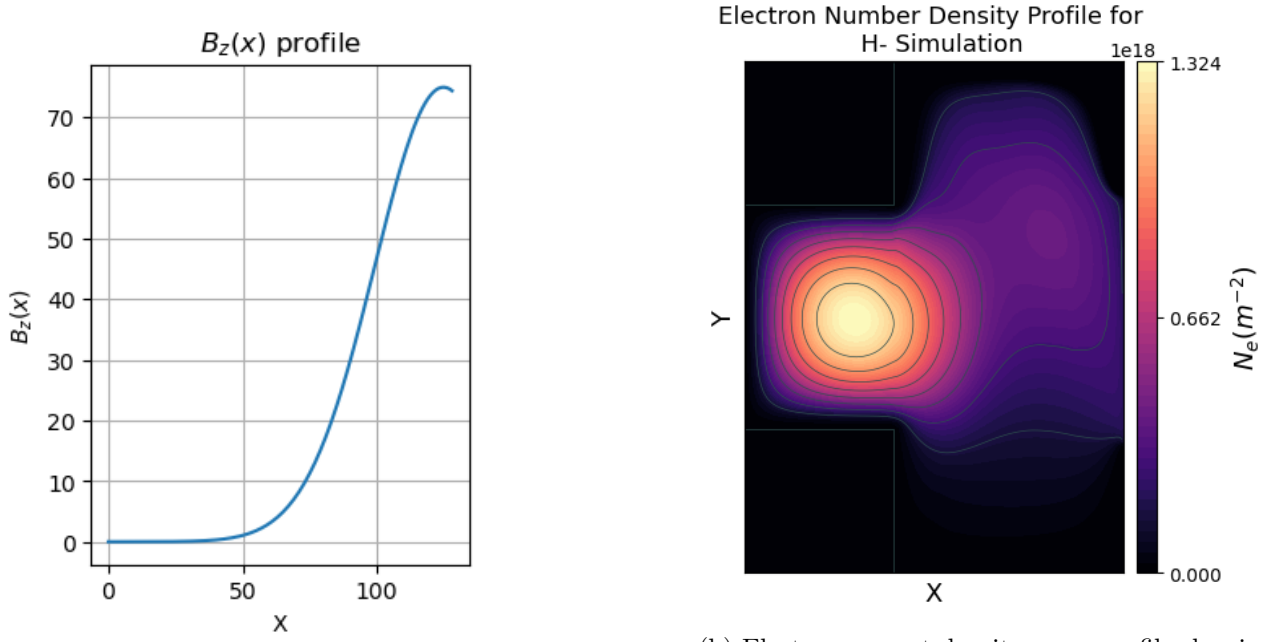

(a) 1D magnetic field profile, $B_z(x)$.

(b) Electron current density or n_e profile showing asymmetry.

Figure 1.4: Illustration of the Hall-like drift. (a) shows the Gaussian-filtered magnetic field $B_z(x)$ across the chamber width. (b) shows the resulting asymmetry in electron transport.

Figure 1.4a shows a 1D profile of the magnetic filter field $B_z(x)$, oriented along the z-axis (into the simulation domain screen) and varying along the x-direction. The profile exhibits a Gaussian-like shape, representing a spatially localized magnetic filter commonly used in plasma confinement systems to modify electron transport. Figure 1.4b displays the electron density n_e distribution in the XY plane. As a result of the applied filter field $B_z(x)$, a clear asymmetry in electron density forms—indicative of Hall-like drifts. Electrons experience an $\mathbf{E}\times\mathbf{B}$ drift due to the combination of the magnetic filter and any present electric field, leading to the off-axis peak in density. This behavior is predicted by the classical drift velocity expression shown in Equation B.2, which describes the perpendicular motion of charged particles in the presence of crossed electric and magnetic fields. This highlights the role of transverse magnetic fields in shaping transport behavior in magnetized plasma systems.

1.6 Negative Ion Dynamics

Negative ion transport behavior is strongly influenced by applied electric and magnetic fields, which govern their motion via the Lorentz force [4]. In magnetized plasmas, charged particles experience gyromotion—circular motion perpendicular to the magnetic field—characterized by a radius known as the Larmor radius:

$$r_L = \frac{v_\perp}{|\Omega|}, \tag{1.7}$$

where $\Omega = \frac{qB}{m}$ is the cyclotron frequency.

Due to their relatively large mass compared to electrons, negative ions tend to exhibit significantly larger Larmor radii under typical operating conditions. As a result, they are often only weakly magnetized, especially in low-field regions of the discharge. This dynamic leads to transport regimes where ions may respond more to electric field gradients and neutral collisions than to magnetic confinement.

In later chapters, we examine this behavior using particle-in-cell simulations, focusing on local ion densities, current transport directions, and the relative magnetization of species. A detailed pointwise analysis is carried out at locations of peak ion density to better understand how negative ions flow through the source and how these flows relate to plasma production and extraction. These studies provide insight into the distinct roles that mass, charge, and field strength play in shaping ion trajectories and confinement within the source.

Chapter 2

Mass Effects on Ion Source Plasma Dynamics

2.1 Introduction

The plasma discharge of a negative ion source was modeled using a two-dimensional electrostatic Particle-in-Cell (PIC) code with Monte Carlo Collisions (MCC). The simulation domain was configured to capture the key features of the ion source geometry, electric field structure, particle dynamics, and relevant physical processes such as collisions, particle heating, and magnetic confinement.

The code was parallelized using hybrid MPI/OpenMP parallelism, with 2 MPI threads and 48 OpenMP threads utilized during the run. This hybrid setup facilitated efficient domain decomposition and concurrent particle pushing and field solving, which was critical given the large number of simulated macroparticles.

The vacuum permittivity ε_0 was rescaled with a factor $k_{\varepsilon_0} = 36000$, consistent with typical practices in PIC codes to enhance numerical stability while preserving physical dynamics. The simulation grid consisted of 128×192 cells, spanning a physical domain from $x = 0.0$ cm to $x = 16.0$ cm, and $y = 0.0$ cm to $y = 58.0$ cm. A central hole of radius 0.91 cm was included to represent the extraction aperture.

The simulation included electrons (e^-), molecular ions (H_2^+), negative ions (H^-), triatomic ions (H_3^+), and protons (H^+). Initial particle populations were as follows:

- Electrons: 379,296
- H_2^+: 170,501
- H^-: 0
- H_3^+: 94,810
- H^+: 114,116

Particles were loaded uniformly up to the maximum grid index $n_x = 129$. While electrons were sampled from a Maxwellian velocity distribution, their velocities were subsequently adjusted, likely due to the heating routine or boundary conditions applied.

The computed Debye length was $\lambda_{De} \approx 6.31$ mm. The grid spacing was $dx = 3.13$ mm and $dy = 3.02$ mm, yielding $dx/\lambda_{De} = 0.495$ and $dy/\lambda_{De} = 0.479$, which are sufficient to resolve electrostatic field structures. The timestep was set to $\Delta t = 5.78 \times 10^{-10}$ s, ensuring $\omega_{pe}\Delta t = 0.102$ and $v_{te}\Delta t/dx = 0.3$, both within stable operational ranges for explicit PIC schemes.

A Gaussian-shaped magnetic filter field with a peak strength of $B_m = 75$ G was applied. The electron gyrofrequency was $\omega_c = 1.32 \times 10^9$ s^{-1}, giving $\omega_c \Delta t = 0.76$. The corresponding Larmor radius was $r_e = 1.19$ mm. The key dimensionless parameters governing dynamics were $\omega^*/\omega_c = 0.96$ and $r^*/r_e = 1.07$, indicating accurate resolution of magnetized electron orbits.

A total of 61 chemical reactions were included, accounting for elastic scattering, ionization, recombination, and excitation processes. The collision subroutine was invoked every 10 timesteps, and the electron heating routine every 4 timesteps. The absorbed power profile was of the flattop type, and heating was distributed throughout the domain.

The Poisson equation was solved using the direct solver PARDISO [1], which reordered and factorized the matrix with approximately 883,791 non-zero elements. The solver achieved a factorization performance of 74 MFLOPS. The number of macroparticles per unit area was $N_m \approx 5.29 \times 10^{10}$.

The electron thermal velocity was $v_{th,e} \approx 1.57 \times 10^6$ m/s and the mean electron speed was $\langle |v| \rangle \approx 1.77 \times 10^6$ m/s. These values are consistent with the electron temperatures expected under the applied heating conditions.

Simulations were run for 3.5 hours until convergence was reached. Output data were saved at regular intervals and subsequently processed into multidimensional Python arrays for analysis. This enabled spatial and species-resolved investigation of ion behavior and volumetric production rates.

A comparative analysis of H^- and D^- ion production within the inductively coupled plasma (ICP) discharge source was conducted. This involved a multi-step computational workflow. Simulation output files were organized into two sets—one for hydrogen and one for deuterium cases. A custom Python script was developed to parse and align these files into 2D spatial grids. The script verified consistency in grid dimensions, allowed for optional normalization, and enabled direct comparison between species. For each quantity analyzed, corresponding hydrogen and deuterium data files were matched by filename. The script ensured compatibility of the grids and performed a pixel-wise computation of the absolute difference between the datasets. This allowed for detailed spatial comparison of ion densities, energy distributions, and production characteristics across isotopic cases.

2.2 Results

This analysis focused on key parameters within the ion source, specifically the number density (n, m^{-3}), the flux (Γ, A/m^2) of H^- ions, and the electric potential (ϕ, V). Maximum values obtained from each simulation were calculated and summarized in Table 2.1, offering a direct comparison of important plasma metrics.

Parameter	**Hydrogen Max**	**Deuterium Max**	**Units**
`Ion Density` (N_i)	5.09×10^{16}	4.63×10^{16}	m^{-3}
`Ion Flux` (Γ_i)	4.46×10^{20}	2.55×10^{20}	A/m^2
`Electric Potential` ($\Phi(V)$)	41.33	37.69	V

Table 2.1: Maximum values of Hydrogen and Deuterium for selected files.

Number Density

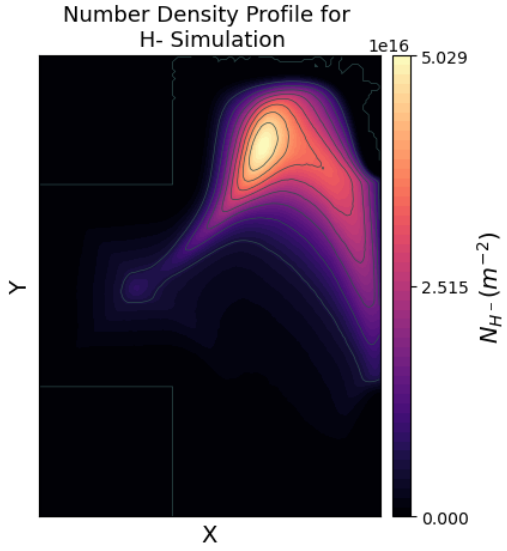

(a) Number Density of Hydrogen Simulation

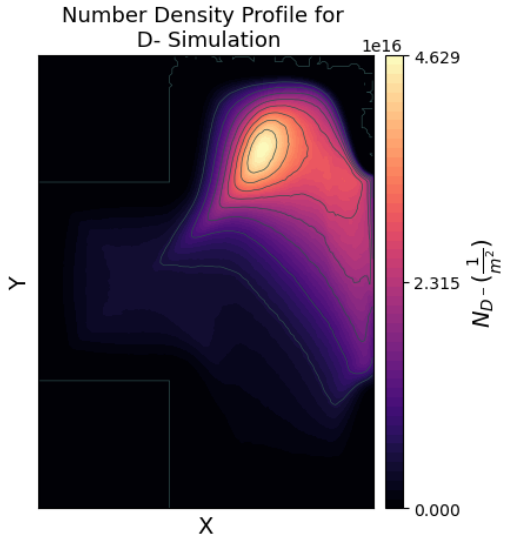

(b) Number Density of Deuterium Simulation

Figure 2.1: Comparison of the number density distributions for hydrogen and deuterium simulations. The maximum number density for the hydrogen simulation is calculated to be $N_{H-} = 5.09 \times 10^{16}\,\mathrm{m}^{-3}$, while for the deuterium simulation, it is $N_{D-} = 4.63 \times 10^{16}\,\mathrm{m}^{-3}$.

Figure 2.1 shows the number density distributions from two Particle-in-Cell simulations: 2.1a for hydrogen negative ion (H^-) production and 2.1b for deuterium negative ion (D^-) production. The simulations were carried out with identical initial conditions, differing only by the ion mass, which was doubled for deuterium to reflect the physical mass difference. The resulting spatial distributions are remarkably similar, with both cases displaying a concentrated region of high density near the upper central portion of the extraction aperture. This structural agreement suggests that, under matched plasma conditions, the overall confinement and extraction dynamics of H^- and D^- ions are governed by similar physical processes. The maximum number densities are calculated to be $N_{\mathrm{H}^-} = 5.09 \times 10^{16}\,\mathrm{m}^{-3}$ for hydrogen and $N_{\mathrm{D}^-} = 4.63 \times 10^{16}\,\mathrm{m}^{-3}$ for deuterium—values that are close in magnitude and further underscore the similarity in behavior. These results indicate that isotopic substitution alone, without additional changes in external fields or boundary conditions, does not significantly alter number density profiles across H- and D- simulations.

Ion Flux

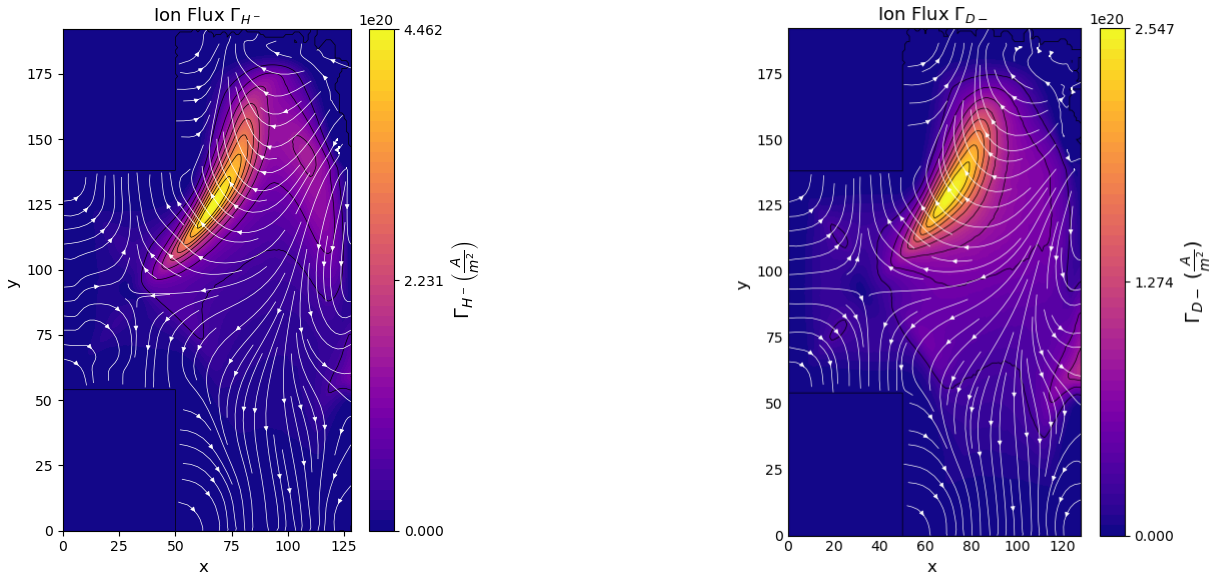

(a) Hydrogen Ion Flux

(b) Deuterium Ion Flux

Figure 2.2: Comparison of the ion flux distributions for hydrogen and deuterium simulations. The maximum ion flux for the hydrogen simulation is calculated to be $\Gamma_{H-} = 4.46 \times 10^{20}\,\mathrm{A\,m^{-2}}$, while for the deuterium simulation, it is $\Gamma_{D-} = 2.55 \times 10^{20}\,\mathrm{A\,m^{-2}}$.

Figure 2.2 presents the ion flux distributions for hydrogen (H^-) and deuterium (D^-) simulations. Both simulations use the same initial plasma conditions, with ion mass being the only difference—doubled in the deuterium case to reflect its physical properties. The flux patterns in both figures exhibit similar overall structure, with ions accelerating toward the extraction aperture and forming a well-defined outflow region. Streamlines indicate that the bulk ion motion is governed by consistent electric field and plasma dynamics in both cases.

Despite the structural similarity, a significant difference is observed in the magnitude of ion flux. The maximum flux for the hydrogen simulation is calculated to be $\Gamma_{\mathrm{H^-}} = 4.46 \times 10^{20}\,\mathrm{A\,m^{-2}}$, while the deuterium simulation reaches a lower peak value of $\Gamma_{\mathrm{D^-}} = 2.55 \times 10^{20}\,\mathrm{A\,m^{-2}}$.

Electric Potential

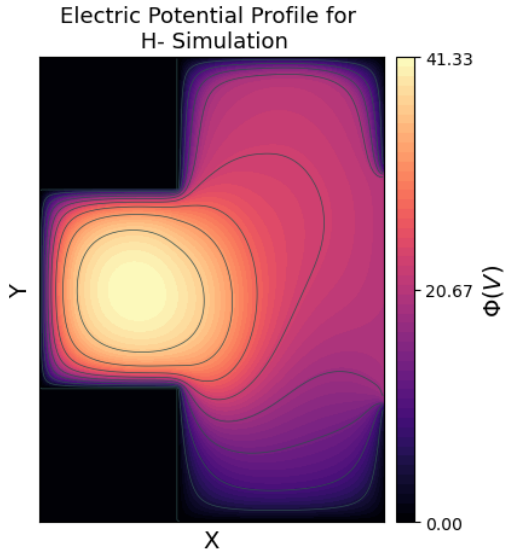

(a) Electric Potential with ICP inlet with Hydrogen gas

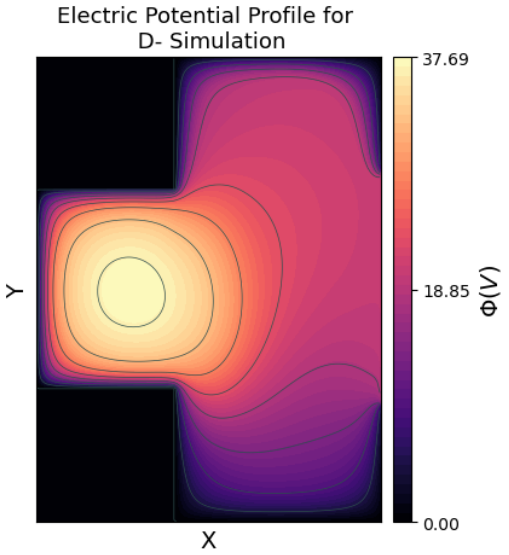

(b) Electric potential with ICP intel with Deuterium gas

Figure 2.3: Comparison of the electric potential distributions for hydrogen and deuterium simulations. The maximum potential for the hydrogen simulation is calculated to be $\Phi_{H-} = 41.33, \mathrm{V}$, while for the deuterium simulation, it is $\Phi_{D-} = 37.69\,\mathrm{V}$.

Figure 2.3 displays the electric potential profiles for simulations using hydrogen and deuterium gas. Both cases were run under identical input parameters and boundary conditions, with the only difference being the ion mass. The resulting potential distributions are strikingly similar in shape and structure, with both exhibiting a central potential well surrounded by smooth, symmetric gradients toward the extraction region. This close agreement indicates that the large-scale electrostatic behavior of the discharge is largely independent of ion mass when all other conditions are held constant.

While the overall form of the potential is nearly identical, a slight difference is observed in the maximum values. The hydrogen case reaches a peak of $\Phi_{\mathrm{H}} = 41.33\,\mathrm{V}$, while the deuterium case reaches $\Phi_{\mathrm{D}} = 37.69\,\mathrm{V}$. Despite this minor variation, the consistency in spatial features reinforces the robustness of the simulation framework and suggests that key aspects of potential formation in RF ion sources are relatively insensitive to isotopic substitution.

Negative Ion Production Source Terms

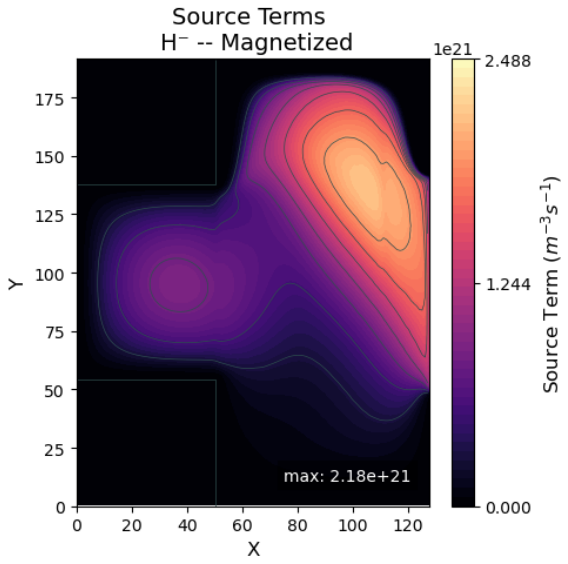

(a) H^- production source terms with ICP inlet using hydrogen gas.

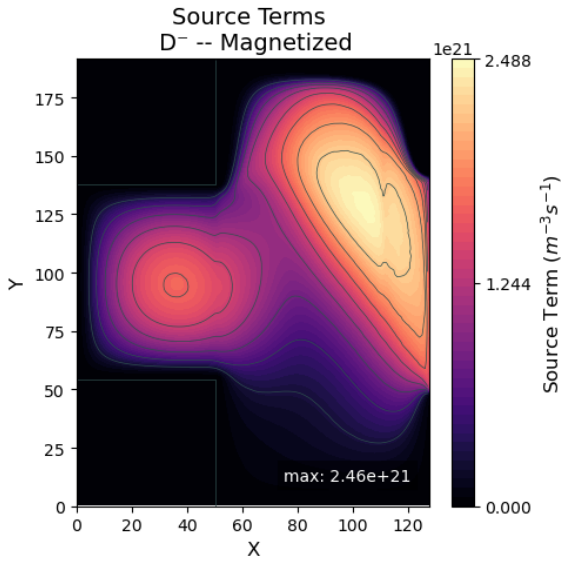

(b) H^- production source terms with ICP inlet using deuterium gas.

Figure 2.4: Simulated negative ion production source terms ζ for H^- and D^- in magnetized configurations. The source terms represent volumetric rates of negative ion production in the plasma chamber. Both cases exhibit spatial asymmetries influenced by the applied magnetic filter field and gas species. The peak production rate in the hydrogen case is $\zeta_{H^-} = 2.18 \times 10^{21}\,\mathrm{m^{-3}s^{-1}}$, while for deuterium it reaches $\zeta_{D^-} = 2.46 \times 10^{21}\,\mathrm{m^{-3}s^{-1}}$.

Figure 2.4 presents the spatial distribution of negative ion production source terms ζ for both H^- and D^- in magnetized conditions. The contour plots reveal distinct spatial structures for the two isotopes, with source term intensities concentrated near the upper right region of the chamber in both cases. However, the D^- profile appears slightly broader and more diffuse, suggesting a difference in confinement or transport behavior compared to hydrogen. These distributions are shaped by the interplay between the inductively coupled plasma (ICP) source, electron temperature gradients, and the imposed magnetic field, which affects electron mobility and thereby influences the rate of dissociative attachment. The maximum source term values—$\zeta_{H^-} = 2.18 \times 10^{21}\,\mathrm{m^{-3}s^{-1}}$ and $\zeta_{D^-} = 2.46 \times 10^{21}\,\mathrm{m^{-3}s^{-1}}$.

2.3 Discussion

Both Figure 2.1 and Figure 2.3 present 2D PIC simulation results for the number densities of negative hydrogen and deuterium ions, along with their respective electric potential profiles within the discharge region. The simulations predict nearly identical number density distributions for the two ion species, indicating that, under matched initial conditions, the overall confinement and accumulation of H^- and D^- ions are governed by similar physical processes.

Similarly, the electric potential profiles exhibit strong structural agreement, with both cases forming a central potential well and comparable gradients toward the extraction boundary. These results suggest that the large-scale electrostatic structure of the discharge is relatively insensitive to ion mass when other conditions remain constant. While minor differences exist in the peak values of number density and electric potential, the spatial features remain consistent between the two cases. This reinforces the idea that isotopic substitution alone does not significantly alter the qualitative characteristics of the plasma under RF-driven operation. Figure 2.1 and Figure 2.3 show that the PIC solution predicts the following outcomes:

$$U(x,y) = q \cdot \phi(x,y)$$

$$U_{\mathrm{H}^-} = K_{\mathrm{H}^-}$$

$$U_{\mathrm{D}^-} = K_{\mathrm{D}^-}$$

$$n_{H-} \approx n_{D-}$$

Since kinetic energy is given by:

$$K_{\mathrm{H}^-} = \frac{1}{2} m_{\mathrm{H}^-} v_{\mathrm{H}^-}^2, \quad K_{\mathrm{D}^-} = \frac{1}{2} m_{\mathrm{D}^-} v_{\mathrm{D}^-}^2$$

we can solve for the velocities of the hydrogen and deuterium negative ions:

$$v_{\mathrm{H}^-} = \sqrt{\frac{2U_{\mathrm{H}^-}}{m_{\mathrm{H}^-}}}, \quad v_{\mathrm{D}^-} = \sqrt{\frac{2U_{\mathrm{D}^-}}{m_{\mathrm{D}^-}}}$$

These expressions show that the velocity of an ion is inversely proportional to the square root of its mass, i.e.,

$$v \propto \frac{1}{\sqrt{m_{\mathrm{ion}}}}$$

Which highlights the expected reduction in velocity for deuterium compared to hydrogen due to its larger mass. Recalling the expression for ion flux:

$$\Gamma = n_i v_i$$

Table 2.2: Summary of variables used in the kinetic and flux equations.

Symbol	**Definition**	**Units**
$U_{\mathrm{H}^-}, U_{\mathrm{D}^-}$	Potential energy of H^- / D^- ions	J (Joules)
$K_{\mathrm{H}^-}, K_{\mathrm{D}^-}$	Kinetic energy of H^- / D^- ions	J (Joules)
$m_{\mathrm{H}^-}, m_{\mathrm{D}^-}$	Mass of H^- / D^- ions	kg
$v_{\mathrm{H}^-}, v_{\mathrm{D}^-}$	Velocity of H^- / D^- ions	m/s
Γ	Ion flux ($\Gamma = nv$)	$\mathrm{A/m^2}$
n	Ion number density	$\mathrm{m^{-3}}$

Table 2.2 shows a description if the mathematical variables and their respective units. We can take the ratio of the fluxes for hydrogen and deuterium:

$$\frac{\Gamma_{H^-}}{\Gamma_{D^-}} = \frac{n_{H^-} v_{H^-}}{n_{D^-} v_{D^-}} \approx \frac{v_{H^-}}{v_{D^-}}.$$

Assuming both species are accelerated through the same potential (i.e., have equal kinetic energy), their velocities are related by the inverse square root of their masses:

$$\frac{v_{H^-}}{v_{D^-}} = \sqrt{\frac{m_{D^-}}{m_{H^-}}} = \sqrt{2}.$$

The key theoretical relationship for comparing fluxes under the assumption of equal kinetic energy and similar ion densities is:

$$\frac{\Gamma_{H^-}}{\Gamma_{D^-}} \approx \sqrt{\frac{m_{D^-}}{m_{H^-}}} = \sqrt{2} \tag{2.1}$$

From the simulation results, the peak ion flux for H^- was approximately 4.4×10^{20} A/m^2, while for D^- it was 2.3×10^{20} A/m^2. Taking the ratio gives:

$$\frac{\Gamma_{H^-}}{\Gamma_{D^-}} \approx \frac{4.4 \times 10^{20}}{2.3 \times 10^{20}} \approx 1.91 \tag{2.2}$$

This result exceeds the expected value of $\sqrt{2} \approx 1.414$, suggesting a discrepancy between the model assumption and the observed behavior.

Figure 2.1 highlights the difference in spatial variation of number densities. Figure 2.1a shows the number density of H^- ions within the discharge. It can be observed that the hydrogen simulation exhibits a higher density confined to a smaller region of high concentration. In contrast, Figure 2.1b shows that the ion density is slightly lower while being more dispersed throughout the discharge.

To further analyze the spatial variation in negative ion number density, additional simulations were performed in which the magnetization of negative ions was deliberately omitted. This approach isolates the influence of magnetic fields within the discharge region on ion transport and flux behavior. Given that hydrogen and deuterium ions are significantly more massive than electrons, their response to magnetic fields is relatively weak. In contrast, electrons—being much lighter—are strongly influenced by the magnetic field and must remain magnetized in the simulation to preserve physical accuracy. By adjusting the simulation algorithm to exclude the magnetic field effects on negative ions while retaining electron magnetization, we can more clearly assess the role of the magnetic filter field in shaping ion density profiles and extraction characteristics [1].

Chapter 3

Effect of Zero Magnetization of Negative Ions

3.1 Introduction

Role of Magnetization and the Magnetization-Off Simulation Strategy

Charged particle dynamics in plasma are governed by the Lorentz force Equation (1.2), where both electric and magnetic fields determine particle acceleration

The magnetic component of the force induces a helical gyromotion around field lines, characterized by the Larmor radius r_L in Equation (1.7)

where m is the particle mass, $v_\perp$ is the component of velocity perpendicular to the magnetic field, q is the particle charge, and B is the magnetic field strength. The extent of magnetization is determined by comparing r_L to a system length scale L: if $r_L \ll L$, the particle is strongly magnetized; if $r_L \gg L$, the particle is weakly magnetized and follows paths dominated by electric forces.

In volume-cusp negative ion sources, magnetic filter fields are applied in the expansion chamber to suppress fast electrons from reaching the extraction region. These fields reduce electron temperature and enhance H^- or D^- production by limiting destructive detachment collisions. Electrons, due to their low mass, are strongly magnetized and experience substantial deflection via $\vec{v} \times \vec{B}$ forces. In contrast, negative ions possess much higher mass-to-charge ratios, resulting in Larmor radii often exceeding characteristic device scales—rendering them weakly magnetized under typical operating conditions.

To quantify the influence of magnetic confinement on negative ion transport, a modified simulation strategy was employed in which the magnetic force term ($\vec{v} \times \vec{B}$) was selectively removed for H^- and D^- ions. This "magnetization-off" approach provides a physically motivated perturbation test, allowing a direct comparison of ion behavior with and without the influence of the magnetic field.

By isolating magnetization effects, this method enables a detailed evaluation of:

- How magnetic fields alter negative ion trajectories and spatial confinement,
- Mass-dependent differences in magnetized behavior (i.e., H^- vs. D^-),
- The role of magnetic forces in shaping the velocity distribution and extraction potential profiles.

To revise the simulation code and prevent the effect of magnetization on negative ions, the script responsible for updating particle positions based on computed fields and velocities from the previous time step was modified. The adjustment ensures that the velocities of negative ions are not influenced by the magnetic fields.

Listing 3.1: Turning off magnetization for specific particle types in Fortran

```
! Positive ions not magnetized
if( flag_B_pos.eq.1 .and. charge(ptype).gt.0.d0 ) flag_B_tmp=0

!!! TMP
if(ptype.eq.3) flag_B_tmp = 0 ! * = 3 indicates negative hydrogen
!!!
```

Results from simulations with zero magnetization for negative ions are shown below:

Parameter / File	**Hydrogen Max**	**Deuterium Max**	**Units**
`Ion Density` (N_i)	5.09×10^{16}	4.63×10^{16}	m^{-3}
`Ion Flux` (Γ_i)	4.46×10^{20}	2.55×10^{20}	$\mathrm{A/m^2}$
`Electric Potential` (Φ)	41.33	37.69	V
	–– Magnetization Off for Negative Ions ––		
`Number Density` (N_i)	4.05×10^{16}	3.71×10^{16}	m^{-3}
`Ion Flux` (Γ_i)	3.71×10^{20}	2.14×10^{20}	$\mathrm{A/m^2}$
`phi.mco` (Φ)	41.88	37.78	V

Table 3.1: Combined maximum values for Hydrogen and Deuterium species from selected files and simulation outputs.

3.2 Results

Number Density

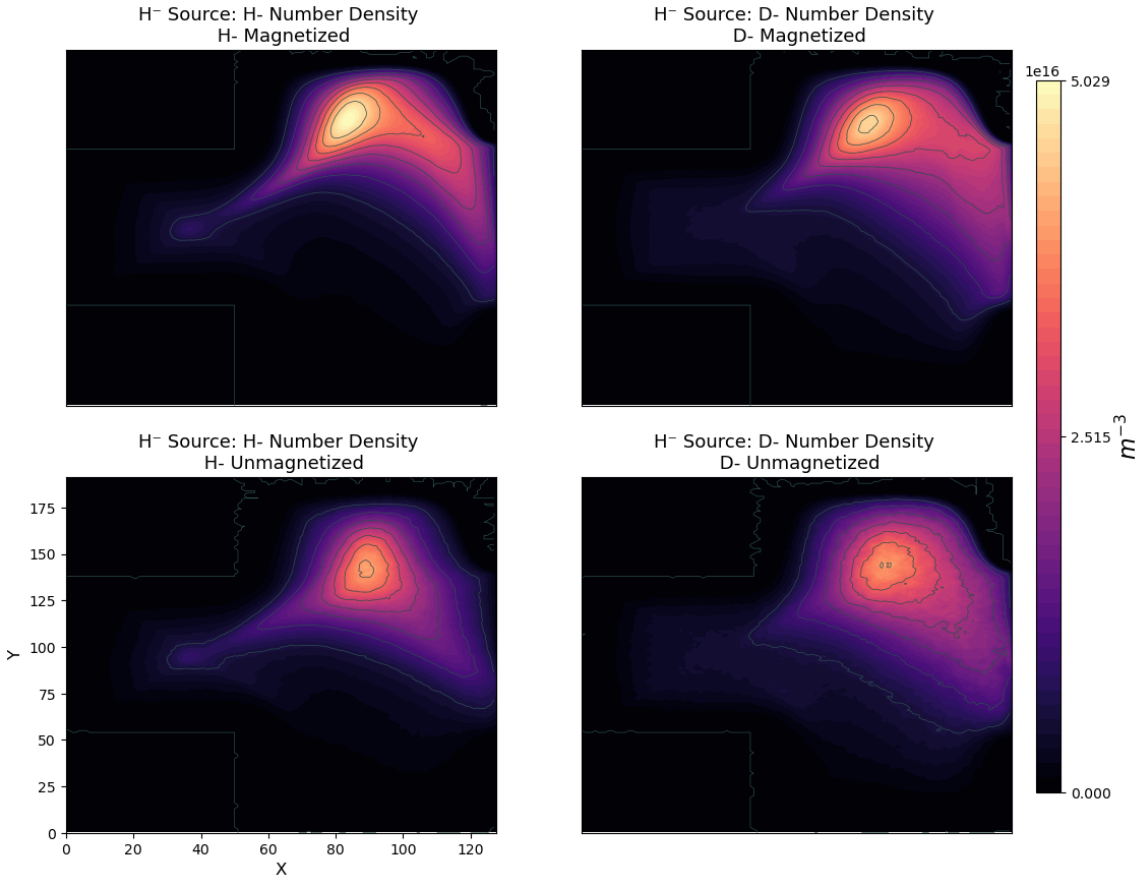

Figure 3.1: Comparison of H/D number density profiles with and without magnetic field adjustments: simulations show distinct confinement and production differences driven by magnetization state

Figure 3.1 presents the number density profiles for H^- and D^- ions from simulations where the magnetic force acting on negative ions was intentionally removed. As in previous simulations, all other parameters remained fixed to allow for an isolated comparison of the ion species under this modified condition. The resulting density distributions retain a broadly similar structure, with the peak densities concentrated near the upper region of the discharge chamber. However, in the absence of magnetization, the spatial extent of the density appears slightly more diffuse, particularly in the case of deuterium.

The maximum number densities are also marginally reduced compared to the magnetized case, with the hydrogen simulation reaching $N_{H^-} = 4.05 \times 10^{16}\,\mathrm{m}^{-3}$, and the deuterium simulation reaching $N_{D^-} = 3.98 \times 10^{16}\,\mathrm{m}^{-3}$. These results suggest that magnetic confinement plays a modest but noticeable role in shaping the spatial distribution and retention of negative ions, particularly in the denser regions near the source aperture.

Electric Potential

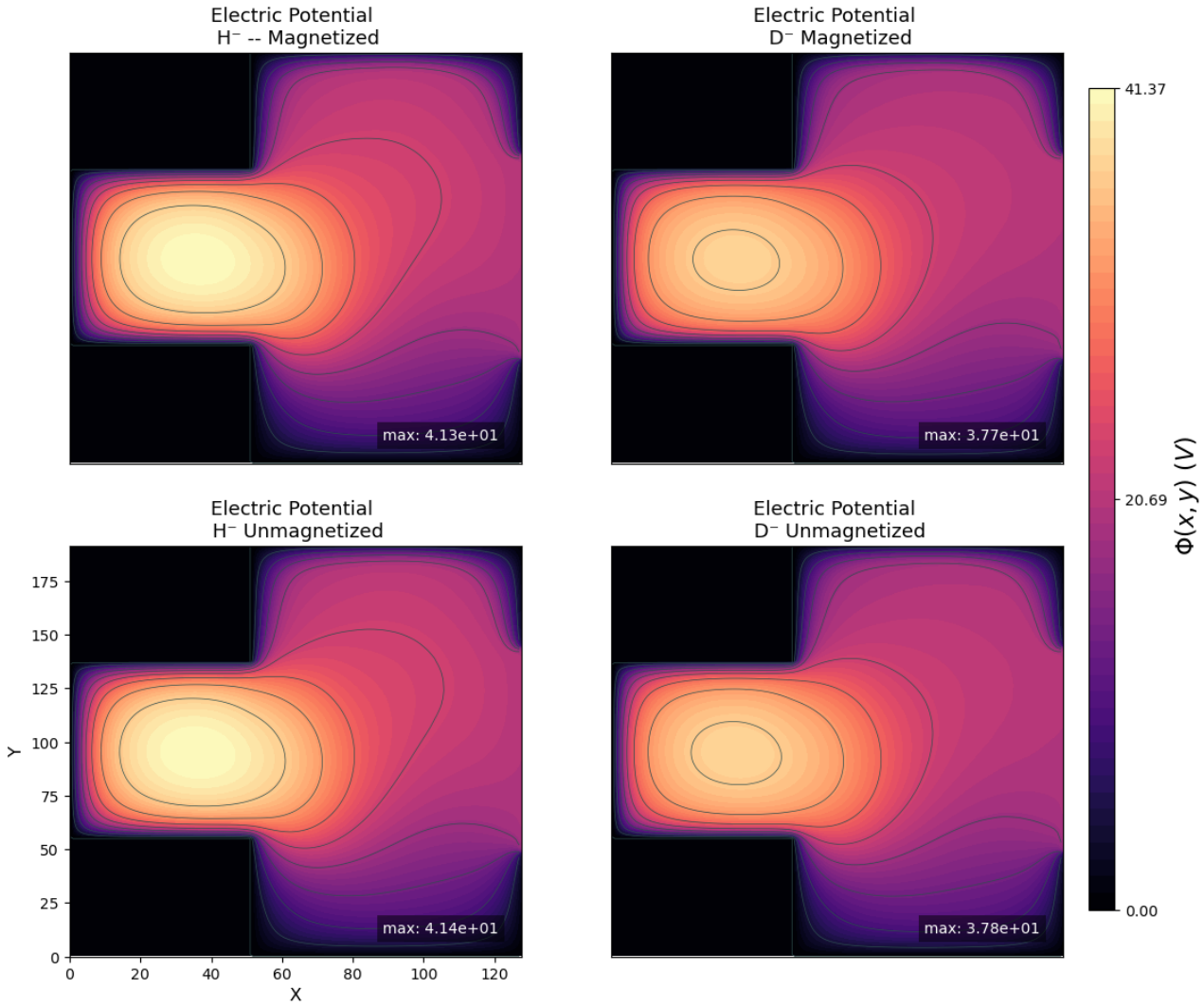

Figure 3.2: Comparison between H-/D- Electric Potential – Magnetization Off.

Figure 3.2 presents the electric potential profiles for hydrogen and deuterium simulations in the absence of magnetic forces acting on negative ions. Both simulations were conducted under otherwise identical initial and boundary conditions, allowing a direct comparison of isotopic effects under unmagnetized conditions. The overall structure of the electric potential remains highly consistent between the two cases, with each exhibiting a centrally located potential well and smooth radial gradients extending toward the chamber boundaries. This consistency further supports the conclusion that the electrostatic structure of the discharge is largely governed by external fields and charge neutrality rather than by the specific properties of the ion species.

Quantitatively, the peak potential in the hydrogen simulation reaches $\Phi_{\mathrm{H}} = 41.37\,\mathrm{V}$, while the deuterium simulation reaches a slightly lower value of $\Phi_{\mathrm{D}} = 37.78\,\mathrm{V}$. Despite this small difference, the spatial agreement across both cases highlights the robustness of potential formation in RF discharges—even when magnetic confinement of negative ions is disabled.

Ion Flux

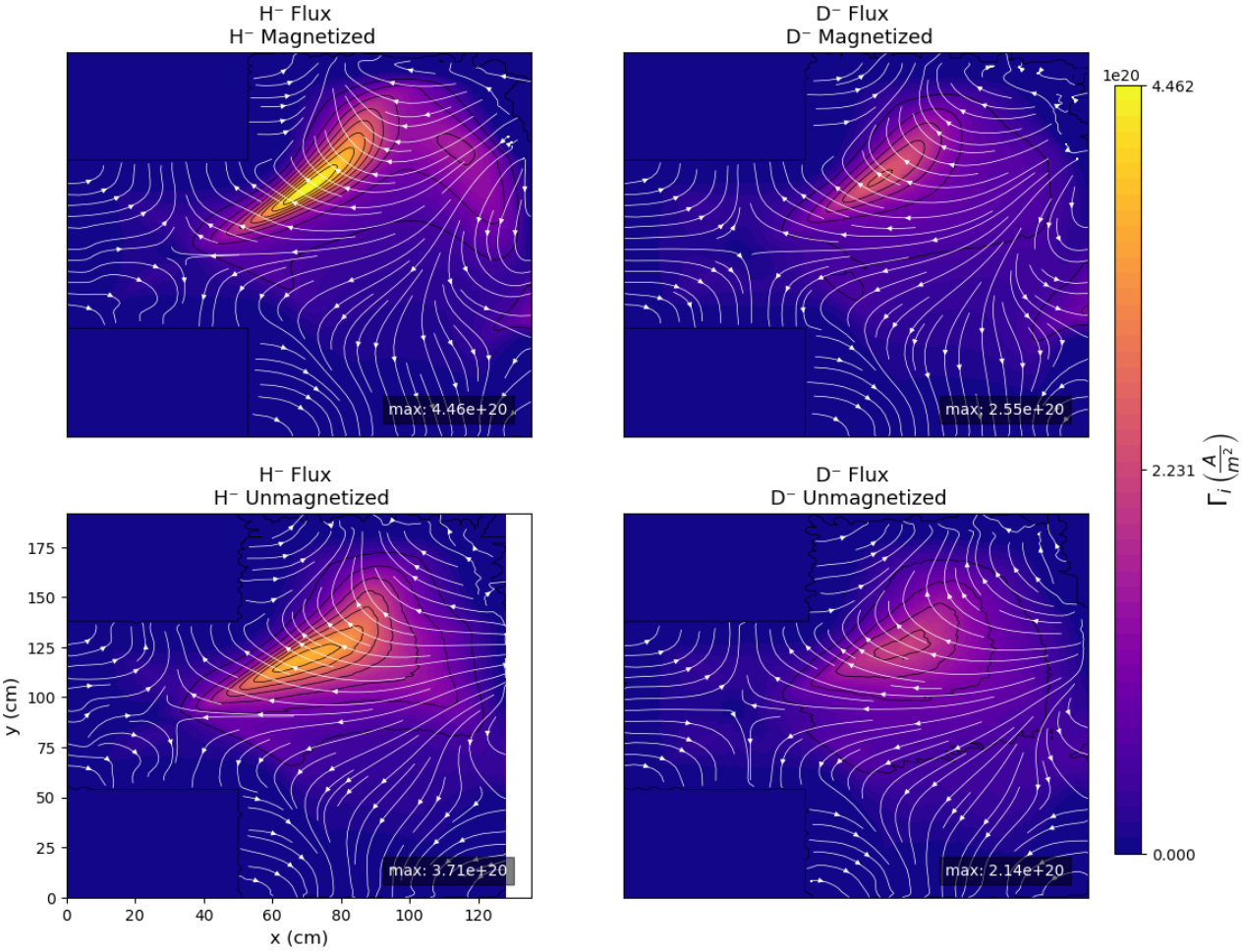

Figure 3.3: Comparison between H-/D- Ion Flux – Magnetization On/Off.

Figure 3.3 shows the ion flux profiles for hydrogen and deuterium simulations with magnetization effects disabled for negative ions. The general structure of the flux remains consistent with earlier results, featuring a concentrated region of ion outflow directed toward the extraction aperture. Streamlines overlaid on the colormap indicate that ion trajectories are still guided by the imposed electric fields, and the bulk flow direction is qualitatively similar between both isotopes.

However, a notable quantitative difference is observed in the peak ion flux values. The maximum hydrogen ion flux reaches $\Gamma_{H^-} = 3.71 \times 10^{20}\,\mathrm{A\,m^{-2}}$, while the deuterium case peaks at $\Gamma_{D^-} = 2.55 \times 10^{20}\,\mathrm{A\,m^{-2}}$. This reduction in flux magnitude for deuterium is consistent with its greater mass, which results in slower acceleration under identical electric fields. The results demonstrate that even in the absence of magnetic confinement, isotopic effects still play a measurable role in determining ion transport efficiency and extraction performance.

3.3 Discussion

Flux Comparison

By removing the effect of magnetization on negative ions within the simulated plasma chamber, an overall decrease in number density was observed for both H^- and D^- simulations, with a smaller difference between the two. A similar but less pronounced trend was noted in ion flux, while the electric potential remained relatively unchanged when zero magnetization was enforced for negative ions.

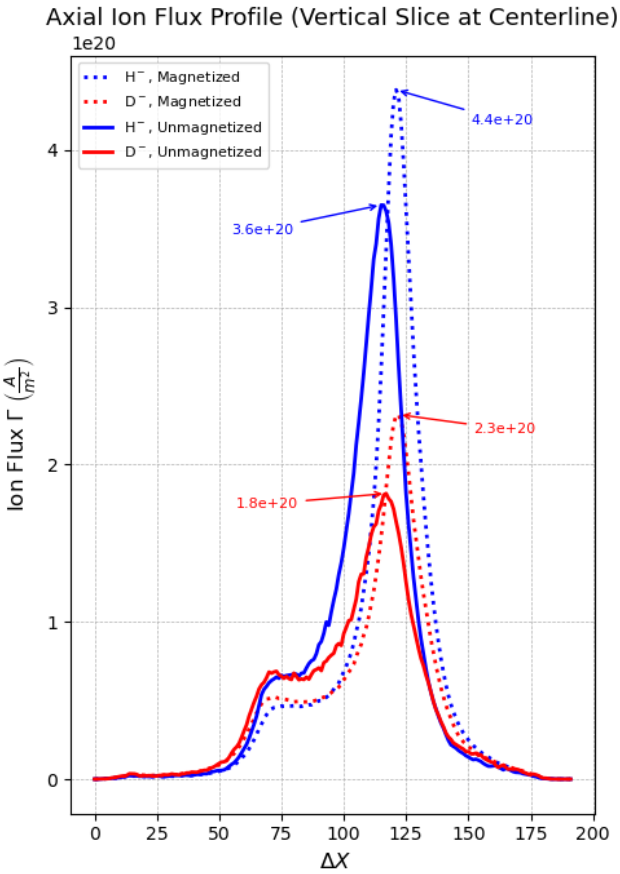

Figure 3.4: Magnetized/Unmagnetized 1D Flux Profiles

As shown in Figure 3.4, the axial ion flux profile at the chamber centerline is plotted for both H^- and D^- simulations, comparing scenarios in which negative ions are either magnetized or unmagnetized. In agreement with trends observed in the number density, the removal of magnetic field influence on negative ions leads to a reduction in peak ion flux for both species. Specifically, the peak flux of magnetized H^- ions reaches approximately 4.4×10^{20} $\frac{A}{m^2}$, while the unmagnetized case decreases to 3.6×10^{20} $\frac{A}{m^2}$. Similarly, the D^- ion flux drops from 2.3×10^{20} $\frac{A}{m^2}$ to 1.8×10^{20} $\frac{A}{m^2}$ under the same conditions.

This reduction is attributed to decreased ion confinement and transport efficiency in the absence of magnetization, which limits the guiding of negative ions along magnetic field lines toward the extraction aperture. Notably, the relative difference between H^- and D^- fluxes also diminishes in the unmagnetized scenario, suggesting that magnetization enhances species-specific behavior due to their differing masses and collision cross sections. The overall shape of the flux profiles remains consistent, indicating that the extraction geometry and electric potential continue to dominate the spatial distribution of ion flux, even when magnetization is removed.

Local Analysis of Plasma Properties at Peak Density

To better understand the local plasma behavior within the simulation domain, we performed a pointwise analysis at the location of maximum negative ion number density, denoted $n_3(x, y)$. This diagnostic approach provides insight into the relationship between the local ion population and the associated current transport characteristics.

From the scalar field n_3, we identified the grid index (i, j) corresponding to the global maximum using a simple search over the 2D array:

$$(i, j) = \text{argmax}(n_3).$$

At this location, the corresponding components of the current density vector $\vec{j}_3(x, y)$ were extracted:

$$j_{3,x} = \vec{j}_3(i, j)_x, \qquad j_{3,y} = \vec{j}_3(i, j)_y.$$

The magnitude of the current density was computed using the Euclidean norm:

$$|\vec{j}_3| = \sqrt{j_{3,x}^2 + j_{3,y}^2}.$$

This provides the local current flux density in units of A/m^2. To determine the direction of the local ion transport, we calculated the streamline angle θ relative to the positive x-axis using the two-argument arctangent function:

$$\theta = \tan^{-1}\left(\frac{j_{3,y}}{j_{3,x}}\right).$$

This angle describes the direction of local ion drift in the plane, accounting for both magnitude and sign of the vector components. The resulting values for n_3, $|\vec{j}_3|$, and θ were recorded for interpretation.

Such localized vector analysis complements the global streamline and density plots, enabling more detailed diagnostics of transport behavior, particularly near production hotspots. It is especially useful in regions where magnetic confinement, electrostatic fields, or boundary effects cause anisotropic transport.

Comparison of Larmor Radii for Electrons and Negative Ions

To assess the degree of magnetization in the plasma, we evaluated the Larmor radii of both electrons and negative hydrogen ions (H^-) at a representative point of peak ion density in the domain. The Larmor radius, previously introduced in Section , quantifies the curvature of a charged particle's trajectory in a magnetic field. It is defined as:

$$r_L = \frac{mv_\perp}{qB}$$

where m is the particle mass, $v_\perp$ is the component of velocity perpendicular to the magnetic field B, and q is the particle charge. By expanding the gyrofrequency $\omega_c = \frac{qB}{m}$, we arrive at the above form, which is more convenient for evaluating magnetization in terms of physical constants and measurable quantities.

$$v = \frac{|\vec{j}|}{|q|n},$$

where $\vec{j}$ is the current density vector and n is the particle number density.

Using simulation data extracted at grid index $(i = 142, j = 88)$, the following values were obtained:

- Electron number density: $n_e = 3.793 \times 10^{17}\,\text{m}^{-3}$
- Electron current density: $|\vec{j}_e| = 7.540 \times 10^{20}\,\text{A/m}^2$
- H- number density: $n_{H^-} = 4.052 \times 10^{16}\,\text{m}^{-3}$

- H- current density: $|\vec{j}_{H^-}| = 2.618 \times 10^{20}\,\mathrm{A/m^2}$
- Applied magnetic field: $B = 75\,\mathrm{G} = 0.0075\,\mathrm{T}$

Using the known particle properties $m_e = 9.11 \times 10^{-31}\,\mathrm{kg}$, $m_{H^-} = 1.67 \times 10^{-27}\,\mathrm{kg}$, and $|q| = 1.602 \times 10^{-19}\,\mathrm{C}$, the computed velocities and Larmor radii are:

$$\begin{aligned} v_{H^-} &\approx 4.03 \times 10^4\,\mathrm{m/s}, \qquad & r_{L,H^-} &\approx 5.6\,\mathrm{cm}, \\ v_e &\approx 1.24 \times 10^4\,\mathrm{m/s}, & r_{L,e} &\approx 0.94\,\mathrm{mm}. \end{aligned}$$

These results clearly demonstrate that electrons are strongly magnetized within the applied field, while the negative hydrogen ions remain effectively unmagnetized. This disparity is a direct consequence of the large mass ratio $m_{H^-}/m_e \sim 1836$, and it confirms the expected behavior in a magnetic filter configuration: the magnetic field selectively impedes electron transport while allowing ions to pass more freely.

Chapter 4

Cross-Section Upgrades with Vibrational Mode Analysis

Introduction

Previous experiments investigating collision dynamics in negative ion sources often relied on datasets that are now considered outdated [13]. In order to assess the influence of isotopic mass on negative ion production—it is critical to revisit these models with more accurate and updated cross-section data. Negative ion sources play a vital role in the neutral beam injection systems used to heat thermonuclear plasmas. Among the most crucial processes in this context are vibrationally resolved electron–D_2 collisions, which significantly impact the efficiency of negative ion production, transport, extraction, acceleration, and neutralization. Notably, sources operated with deuterium consistently underperform compared to those using hydrogen under equivalent power and pressure conditions, highlighting a pronounced isotopic dependence driven by nuclear motion in resonant dissociative attachment (DA) channels. This isotope effect has been experimentally investigated in detail by Krishnakumar et al. [16], reinforcing the need for accurate deuterium cross sections in kinetic models. However, due to the limited accessibility of diagnostics in operational fusion sources, experimental characterization of plasma parameters remains challenging. To address this, compact and versatile testbeds like the RAID helicon plasma device offer a controlled environment to replicate the electron temperature and density conditions typical of fusion-relevant negative ion sources [19]. Ongoing particle-in-cell and fluid simulations of RAID discharges aim to validate and refine numerical models [21], particularly in the context of isotope-sensitive transport and plasma chemistry [17, 18, 20].

Structure of the Updated Collision Database

To support these simulation efforts, a structured HDF5 database has been assembled containing updated cross-section data for five key collisional pairs relevant to deuterium plasmas: electron–D, electron–D^+, electron–D_2, electron–D_2^+, and D^+–D. The data originates from recent theoretical and experimental studies and is organized to facilitate direct integration into particle-in-cell (PIC) and fluid simulation codes [14].

Each HDF5 file contains two main top-level groups:

- `species_data` — defines elementary properties of all species involved in the reactions, such as mass, charge, and internal degrees of freedom.
- `collisions_species1_species2` — contains all available reaction channels for a given collisional pair, resolved by initial vibrational or electronic excitation levels.

For collisions involving D_2 (e.g., electron–D_2), the subfolders are labeled by vibrational states, using a format such as `n0v0_n0vX`. This denotes an incoming electron in its ground state (electrons have no vibrational states) colliding with a D_2 molecule in vibrational level $v = 0$, producing a final

state in vibrational level $v = X$. In contrast, for species like D atoms or D^+ ions, which lack internal vibrational structure, the only folder present is `n0v0_n0v0`.

Within each vibrational channel folder, the elementary processes (e.g., vibrational excitation, dissociative attachment, ionization) are stored in separate subfolders. These include standardized datasets:

- `E_thr` — threshold energy of the process (eV),
- `dE_COM` — energy spacing between data points in center-of-mass coordinates,
- `n_points` — number of energy points in the dataset,
- `sigma` — cross section values (in m^2) as a function of energy,
- `products` — species produced by the reaction,
- `n_products` — number of outgoing particles,
- `vib_level_final` — final vibrational state of D_2, if applicable.

The database thus enables a fine-grained representation of energy-resolved collision processes with explicit vibrational-state dependence. This level of detail is critical for accurately modeling isotope-sensitive mechanisms, such as resonant dissociative attachment, where small shifts in vibrational thresholds can lead to substantial changes in reaction rates. Table 4.1 summarizes the primary electron-induced reaction pathways in molecular deuterium (D_2), including vibrational excitation, dissociative electron attachment, and dissociative excitation. These reaction channels form the physical basis for the input files used in simulation, which are programmatically generated as described in the following section.

Label	**Reaction**
Vibrational excitation	
VE1	$e(\epsilon) + D_2(X\,^1\Sigma_g^+;\nu) \rightarrow D_2{}^-(X\,^2\Sigma_u^+, B\,^2\Sigma_g^+, C\,^2\Sigma_g^+) \rightarrow e(\epsilon') + D_2(X\,^1\Sigma_g^+;\nu')$
VE2	$e(\epsilon) + D_2(X\,^1\Sigma_g^+;\nu) \rightarrow D_2{}^-(C\,^2\Sigma_g^+) \rightarrow e(\epsilon') + D_2(B\,^1\Sigma_u^+;\nu')$
VE3	$e(\epsilon) + D_2(B\,^1\Sigma_u^+;\nu) \rightarrow D_2{}^-(C\,^2\Sigma_g^+) \rightarrow e(\epsilon') + D_2(B\,^1\Sigma_u^+;\nu')$
Dissociative electron attachment	
DA1	$e(\epsilon) + D_2(X\,^1\Sigma_g^+;\nu) \rightarrow D_2{}^-(X\,^2\Sigma_u^+, B\,^2\Sigma_g^+) \rightarrow D(1s) + D^-(1s^2)$
DA2	$e(\epsilon) + D_2(X\,^1\Sigma_g^+;\nu) \rightarrow D_2{}^-(C\,^2\Sigma_g^+) \rightarrow D(n=2) + D^-(1s^2)$
DA3	$e(\epsilon) + D_2(B\,^1\Sigma_u^+;\nu) \rightarrow D_2{}^-(C\,^2\Sigma_g^+) \rightarrow D(n=2) + D^-(1s^2)$
Dissociative excitation	
DE1	$e(\epsilon) + D_2(X\,^1\Sigma_g^+;\nu) \rightarrow D_2{}^-(X\,^2\Sigma_u^+, B\,^2\Sigma_g^+, C\,^2\Sigma_g^+) \rightarrow e(\epsilon') + D_2(X\,^1\Sigma_g^+;\epsilon_c) \rightarrow e(\epsilon') + D(1s) + D(1s)$
DE2	$e(\epsilon) + D_2(B\,^2\Sigma_g^+, C\,^2\Sigma_g^+) \rightarrow D_2{}^-(b\,^3\Sigma_u^+;\epsilon_c) \rightarrow e(\epsilon') + D(1s) + D(1s)$
DE3	$e(\epsilon) + D_2(B\,^1\Sigma_u^+;\epsilon_c) \rightarrow e(\epsilon') + D(2p) + D(1s)$
DE4	$e(\epsilon) + D_2(B\,^1\Sigma_u^+;\epsilon_c) \rightarrow e(\epsilon') + D(2p) + D(1s)$
DE5	$e(\epsilon) + D_2(B\,^1\Sigma_u^+;\epsilon_c) \rightarrow e(\epsilon') + D(1s) + D(1s)$
DE6	$e(\epsilon) + D_2(B\,^1\Sigma_u^+) \rightarrow D_2{}^-(C\,^2\Sigma_g^+) \rightarrow e(\epsilon') + D_2(X\,^1\Sigma_g^+;\epsilon_c) \rightarrow e(\epsilon') + D(1s) + D(1s)$

Table 4.1: Electron-induced reaction pathways in D_2 including vibrational excitation, dissociative electron attachment, and dissociative excitation.

Automation of HDF5 Cross-Section Data Conversion

Accurate reaction cross sections are essential for performing realistic Particle-in-Cell with Monte Carlo Collisions (PIC/MCC) simulations of low-temperature plasmas. These datasets are typically stored in HDF5 format, which supports hierarchical organization and accommodates a wide variety of physical parameters, including energy-dependent reaction channels, species labels, and vibrational or excitation states. However, manually extracting and converting this data into simulation-ready formats is both time-consuming and error-prone.

To address this challenge, we developed a Python-based automation pipeline that loads, parses, and exports HDF5 cross-section files into formatted `.dat` files compatible with our simulation framework. The process includes several key steps:

1. **Recursive HDF5 Loading:** A custom function utilizing the `h5py` library recursively traverses the file structure, loading all groups and datasets into a nested Python dictionary. This structure allows for intuitive inspection and flexible access to deeply nested data.

2. **Species and Metadata Parsing:** The filenames encode the identities of the interacting species. Using regular expressions, the relevant species labels are extracted. Additionally, quantum state information—such as initial and final vibrational or excitation levels—is parsed from the reaction keys when available.

3. **Formatted Output Generation:** Each reaction entry is converted into a structured block following the `.dat` format required by the PIC/MCC code. This block includes:

   - A header indicating reactants and products, with appropriate quantum state annotations.
   - The reaction threshold energy (E_{thr}) and a placeholder for center-of-mass energy loss values.
   - A metadata section containing reaction identifiers and references.
   - A tabulated cross-section dataset over a custom energy grid, combining fine low-energy resolution with logarithmic spacing at higher energies.

4. **Batch Export Functionality:** The pipeline supports batch processing of multiple HDF5 files. All converted output files are saved to a user-defined directory, enabling rapid preparation of input files for large simulation campaigns.

This automated approach significantly reduces setup time and minimizes the risk of transcription errors, facilitating more efficient and reproducible simulation workflows. To evaluate the structure and behavior of the cross sections being produced by the database and formatted for simulation, we next present a comparative visualization of three key electron-induced reaction channels. The vibrational levels selected for this analysis—$v' = 5$–10—were chosen to reflect the behavior emphasized in the vibrationally resolved modeling approach of [14], where these modes were shown to contribute most significantly to dissociative attachment, excitation, and dissociation processes under low-temperature plasma conditions. Figure 4.1 displays the corresponding cross sections extracted from the database and reformatted for simulation input, highlighting the energy thresholds, magnitude variation, and resonance structures that characterize each reaction type.

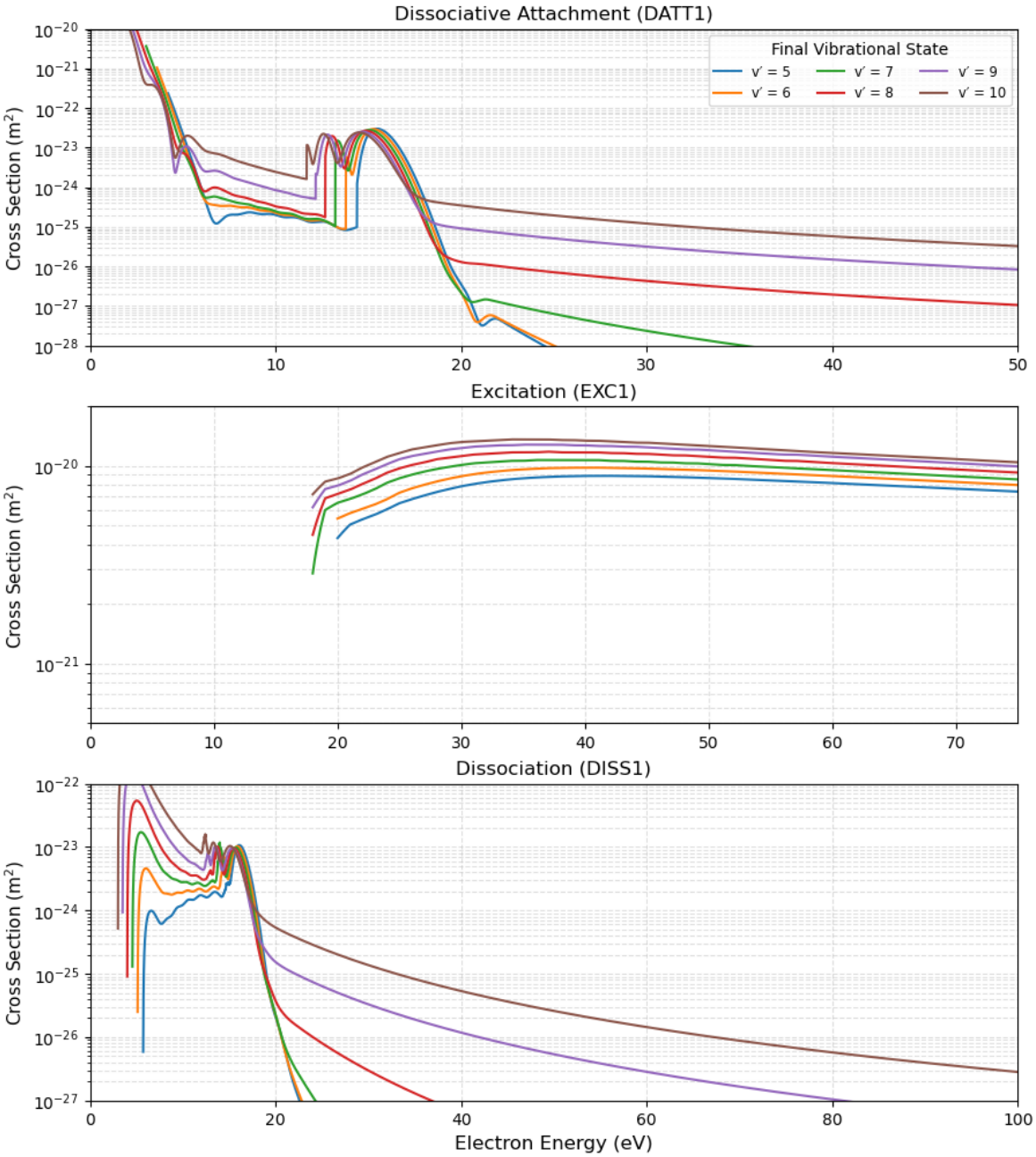

Figure 4.1: Energy-resolved cross sections for electron-induced processes involving vibrationally excited D_2 molecules. Each subplot displays the dependence of a distinct elementary reaction channel on the final vibrational state $v' = 5$–10, starting from $v = 0$. **Top:** Dissociative attachment (DATT1), highlighting vibrational threshold shifts and resonant peaks below 20 eV. **Middle:** Vibrational excitation (EXC1), showing a rapid onset near 18–20 eV followed by saturation. **Bottom:** Dissociation (DISS1), with broad resonance features and strong variation across v' levels. These curves illustrate the isotope- and vibrational-sensitive nature of electron–D_2 collisions relevant to negative ion source modeling.

These vibrationally resolved cross sections form the foundation for improved kinetic modeling of isotope-sensitive behavior in negative ion sources. The strong dependence of dissociative attachment on vibrational state, along with threshold shifts in dissociation and excitation, highlights the importance of including vibrational excitation—especially for deuterium. Integrating these cross sections into the PIC/MCC framework enables more accurate plasma chemistry and improved predictions of negative ion yield under fusion-relevant conditions.

Chapter 5

Final Remarks

5.1 Conclusion

This thesis presented a detailed numerical study of negative ion production in RF-driven ion sources, with a focus on understanding the observed discrepancies between hydrogen (H^-) and deuterium (D^-) performance. Using a two-dimensional electrostatic PIC-MCC simulation code developed by Dr. Gwenael Fubiani, we modeled the ITER BATMAN ion source as a stand-in for the TRIUMF/D-Pace system due to their similar geometries and plasma conditions.

The first part of this work examined the effect of ion mass by simulating H^- and D^- plasmas under otherwise identical conditions. Results showed comparable spatial structures in number density and potential distributions, but consistently lower flux for D^- ions — a difference consistent with theoretical predictions based on ion mass scaling.

To further isolate physical mechanisms, a second set of simulations was performed where the magnetic force on negative ions was deliberately turned off. This allowed a focused investigation into the role of magnetization in negative ion transport. The results demonstrated that while the large-scale electric potential remained largely unchanged, the absence of magnetization led to reduced confinement and a drop in extracted flux, particularly for deuterium.

Recognizing the limitations of outdated cross-section data, the final part of the project involved developing a Python-based automation framework to process updated deuterium cross-sections provided by CNR Bari. This tool converts vibrationally resolved HDF5 datasets into a structured format compatible with simulation codes, enabling future studies to include detailed vibrational dynamics and isotopic effects.

In combination, these simulation results and data-processing tools contribute to a more accurate, physically grounded understanding of isotope-dependent behavior in negative ion sources — supporting both improved modeling and the design of more efficient ion source systems.

5.2 Next Steps

The work presented in this thesis lays the groundwork for a proposed summer research internship, for which a MITACS Accelerate grant has been submitted. If approved, the project will focus on implementing the updated deuterium cross-section data into the PIC-MCC simulation framework and extending this infrastructure to include newly acquired hydrogen cross-section datasets. This would enable a more rigorous and physically meaningful comparison between H^- and D^- production, accounting for isotope-specific reaction pathways and vibrational dynamics.

The proposed research would be conducted under the academic supervision of Dr. Christina Haston, in collaboration with industry partners D-Pace and Accel-Link Ltd., led by Dr. Morgan Dehnel. The project aims to further automate the data integration pipeline, validate simulation results against experimental trends, and explore design considerations that may help address the persistent performance gap between hydrogen and deuterium ion sources.

Appendix A

Derivation of the Vlasov Equation

The progression from the N-body problem to a fluid representation involves a series of simplifications and averaging processes that transition from a microscopic description of individual particles to a macroscopic description of collective plasma behavior [4]. The dynamics of a system of N interacting particles are governed by Newton's equations of motion:

$$m_i \frac{d\mathbf{v}_i}{dt} = \sum_{j \neq i} \mathbf{F}_{ij},$$

where m_i is the mass of the i-th particle, $\mathbf{v}_i$ its velocity, and $\mathbf{F}_{ij}$ the force exerted on particle i by particle j (e.g., Coulomb force for plasmas). Coupled with the equations for the electromagnetic fields, this formulation constitutes the N-body problem. For large N, solving these equations directly becomes computationally infeasible. To simplify the description, we use a statistical approach based on the phase-space distribution function.

Clasically, particles are treated as point-objects with a defined charge and mass. A single particles path can be described by the function $X_1(t)$, in three-dimensional configuration space (x, z, y). Furthermore, a particles orbit can be differentiated with respect to time to obtain a function for the particles velocity.

$$X_1(t) = [x_x(t), x_y(t), x_z(t)]$$
$$V_1(t) = \frac{dX_1}{dt} = \frac{d}{dt}[x_x(t), x_y(t), x_z(t)]$$

To obtain a 6D phase-space we combine the 3D configuration with the 3D velocity space. The density of a single particle can be determined using:

$$N(x, v, t) = \delta[x - X_1(t)]\delta[v - V_1(t)] \tag{A.1}$$

The Dirac delta function $\delta(x)$ is defined as a generalized function (or distribution) such that:

$$\int_{-\infty}^{\infty} \delta(x - a) f(x)\, dx = f(a) \tag{A.2}$$

for any well-behaved test function $f(x)$. It satisfies:

$$\delta(x - a) = 0 \quad \text{for } x \neq a, \quad \text{and} \quad \int_{-\infty}^{\infty} \delta(x - a)\, dx = 1.$$

In the equation for particle density x, v represent cartersian coordinates while X, V correspond to the lagrangian coordinates. Exploring this equation further, it aids to consider a closed system with one gas particle. At a chosen time t, the density of particles integrated over all of phase-space must yield a value of 1 (ie. the number of particles in the system).

$$\int N(x, v, t) d^3v d^3x = 1$$

To obtain this result, starting from the dirac dela formulation of N:

$$\iint \delta[x - X_1(t)]\delta[v - V_1(t)]d^3v d^3x$$

$$\int \delta[x - X_1(t)]d^3x \int \delta[v - V_1(t)]d^3v$$

By definition, $\int \delta[x - X_1(t)] = 1$; validating $\int N(x, v, t)d^3v d^3x = 1$. A general expression of $N(x, v, t)$ can be written as follows:

$$N(x, v, t) = \sum_{s=1}^{s} \delta[x - X_1(t)]\delta[v - V_1(t)]$$

Next, we formulate the lorentz equation in a form that will consider an N-body approach.

$$m_i \dot{V_i}(t) = q_s E^m[X_i(t), t] + \frac{q_s}{c} \dot{V_i}(t) \times B^m[X_i(t), t]$$

E^m and B^m are fields that satisfy maxwells equations:

$$\begin{aligned} \nabla \cdot E^m(x, t) &= 4\pi\rho^m(x, t) \\ \nabla \cdot B^m(x, t) &= 0 \\ \nabla \times E^m &= -\frac{1}{c}\frac{\partial B^m}{\partial t} \\ \frac{4\pi}{e} J^m(x, t) &- \frac{1}{c}\frac{\partial E^m}{\partial t} \end{aligned} \tag{A.3}$$

An exact equation of plasma evoulution can be obtained from the time derivative of $N_s(x, v, t)$

$$\frac{\partial N_s}{\partial t} = -\left[\sum_{i=1}^{i} \dot{X_i}(t) \cdot \nabla_x \delta[x - X_1(t)]\delta[v - V_1(t)] - \sum_{i=1}^{i} \dot{V_i}(t) \cdot \nabla_v \delta[x - X_1(t)]\delta[v - V_1(t)]\right]$$

Using the relationship that $\dot{X_i}(t) = V_i(t)$ and the lorentz formulation we can obtain an exact plasma description known as the Klimontovich equation:

$$\frac{\partial N_s(\mathbf{x}, \mathbf{v}, t)}{\partial t} + \mathbf{v} \cdot \nabla_{\mathbf{x}} N_s + \frac{q_s}{m_s}\left(\mathbf{E}^m + \frac{\mathbf{v}}{c} \times \mathbf{B}^m\right) \cdot \nabla_{\mathbf{v}} N_s = 0. \tag{A.4}$$

The Klimontovich equation contains more information than needed for simulating the desired plasma behavior. Another way to view this equation is by equating it to the continuity equation. Again considering a closed system with one gas particle mass m_s and charge q_s. The single gas particle has an orbit $X_s(t)$ determined by the fields involved. In order to take a time derivative of V_s we must define the "convective" derivative. As demonstrated in [4], the convective derivative $\frac{D}{Dt} N_s(t) = 0$ implying that the number of particles of a given species in a closed system remains constant over time.

$$\frac{D}{Dt} \equiv \frac{\partial}{\partial t} + \left.\frac{dx}{dt}\right|_{\text{orbit}} \cdot \nabla_x + \left.\frac{dv}{dt}\right|_{\text{orbit}} \cdot \nabla_v$$

The continuity equation can be expresses as:

$$\frac{\partial f(r, t)}{\partial t} + \nabla_r \cdot (f\mathbf{V}) = 0$$

Here:

- ∇_r represents the divergence in phase space ($\nabla_r = (\nabla_x, \nabla_v)$).
- $\mathbf{V} = \left(\frac{dx}{dt}, \frac{dv}{dt}\right)_{\text{orbit}}$ is the vector describing the rate of change of a fluid element in phase space.

- $f(r, v, t)$ is an arbitrary function in phase-space.

Since the particle density N_s is conserved, it must satisfy the continuity equation:

$$\frac{\partial N_s(x,v,t)}{\partial t} + \nabla_x \cdot (vN_s) + \nabla_v \cdot \left\{ \frac{q_s}{m_s} \left[\mathbf{E}^m + \frac{\mathbf{v}}{c} \times \mathbf{B}^m \right] N_s \right\} = 0 \tag{A.5}$$

- N_s is the particle density.
- q_s/m_s is the charge-to-mass ratio.
- $\mathbf{v}$ is the velocity, and c is the speed of light.

Given the precise forms of the Klimontovich equation and the continuity equation, our goal is to calculate the plasma's average properties. Using A.4 and A.5 as a foundation, we derive equations that characterize the plasma's average behavior. The Klimontovich equation tells us if a point particle with infinite density will be found at a particular point in phase space. A more useful approach would be to calculate the amount of particles that can be found in a differential volume of phase space $\Delta x \Delta v$. Taking an ensemble average [4] over an infinite amount of realizations allows us to compute the number of particles of a particular species per unit configuration space per unit velocity space.

$$f_s(x,v,t) = \langle N_s(x,v,t) \rangle \tag{A.6}$$

To determine the time evolution of the distribution function $f_s(x, v, t)$, we utilize the Klimontovich equation A.4 and apply ensemble averaging. For this purpose, the quantities δN_s, δE, and δB are defined as follows:

$$\begin{aligned} N_s(x,v,t) &= f_s(x,v,t) + \delta N_s(x,v,t) \\ E^m(x,v,t) &= E(x,v,t) + \delta E(x,v,t) \\ B^m(x,v,t) &= B(x,v,t) + \delta B(x,v,t) \end{aligned}$$

Here, $B = \langle B^m \rangle$, $E = \langle E^m \rangle$, and the ensemble averages satisfy $\langle \delta N_s \rangle = \langle \delta E \rangle = \langle \delta B \rangle = 0$. Substituting these definitions into equation A.4 and performing ensemble averaging provides us with the exact form of the *plasma kinetic equation* A.7.

$$\frac{\partial f_s(x,v,t)}{\partial t} + \mathbf{v} \cdot \nabla_x f_s + \frac{q_s}{m_s} \left(\mathbf{E} + \frac{\mathbf{v}}{c} \times \mathbf{B} \right) \cdot \nabla_v f_s = -\frac{q_s}{m_s} \left\langle \delta\mathbf{E} + \frac{\mathbf{v}}{c} \times \delta\mathbf{B} \right\rangle \cdot \nabla_v \delta N_s, \tag{A.7}$$

The kinetic equation is derived from the plasma kinetic equation, which describes how the distribution function $f(\mathbf{r}, \mathbf{v}, t)$, representing the number density of particles in phase space, evolves over time. The general form of the kinetic equation is given as:

$$\frac{\partial f}{\partial t} + \mathbf{v} \cdot \nabla_{\mathbf{r}} f + \frac{\mathbf{F}}{m} \cdot \nabla_{\mathbf{v}} f = \left(\frac{\partial f}{\partial t} \right)_{\text{coll}},$$

where $\mathbf{F}$ represents the force acting on the particles, and $\left(\frac{\partial f}{\partial t}\right)_{\text{coll}}$ accounts for changes in f due to particle collisions.

To arrive at the Vlasov equation, we consider a collisionless plasma. In this case, the contribution from collisions can be neglected, so the collision term vanishes:

$$\left(\frac{\partial f}{\partial t} \right)_{\text{coll}} = 0.$$

This reduces the kinetic equation to:

$$\frac{\partial f}{\partial t} + \mathbf{v} \cdot \nabla_{\mathbf{r}} f + \frac{\mathbf{F}}{m} \cdot \nabla_{\mathbf{v}} f = 0.$$

In a plasma, the force acting on the particles is dominated by electromagnetic interactions. Using the Lorentz force law 1.2. Substituting this expression for $\mathbf{F}$ into the reduced kinetic equation, we obtain:

$$\frac{\partial f}{\partial t} + \mathbf{v} \cdot \nabla_{\mathbf{r}} f + \frac{q}{m} (\mathbf{E} + \mathbf{v} \times \mathbf{B}) \cdot \nabla_{\mathbf{v}} f = 0. \tag{A.8}$$

This equation, known as the Vlasov equation, describes the time evolution of the distribution function in a collisionless plasma. It accounts for the effects of both the particle motion through space and the forces arising from electric and magnetic fields, making it a cornerstone of plasma physics in the collisionless regime.

Appendix B

Electron Drift Derivation

It has been seen experimentally that the electron drift towards the lateral walls creates a charge seperation within the expansion chamber setting up a transverse electric field analogous to a hall voltage in a semiconductor. We begin with the general expression for the electron flux, given by Equation (20) from [1]

$$\mathbf{\Gamma}_e = -\mu_e \left[\nabla P_e + n_e e\mathbf{E} + \Gamma_e \times \mathbf{B}\right], \tag{B.1}$$

where $\mu_e = \frac{|e|}{m_e \nu_e}$ is the electron mobility, ∇P_e is the gradient of the electron pressure, $n_e\mathbf{E}$ is the electric field contribution, and $\Gamma_e \times \mathbf{B}$ represents the magnetic drift. To Find an equation for Γ_e we start by rewriting B.1 with the expression $\Omega = \frac{\mu B}{m v_m}$

$$\Gamma_e + \Omega \times \Gamma_e = G$$

Then, taking the cross product of both sides of our new expression:

$$[\Gamma_e + \Omega \times \Gamma_e] \times B = G \times B$$

Expanding this out for further simplifications:

$$\Gamma_e \times B + B \times (\Omega \times \Gamma_e) = G \times B$$

Using the triple cross product rule:

$$B \times (\Omega \times \Gamma_e) = (B \cdot \Gamma_e)\Omega - (B \cdot \Omega)\Gamma$$

Plugging the expanded form of $(\Gamma_e \times \vec{B}) \times \vec{B}$ back into our original expression and solving for $(\Gamma_e \times B)$:

$$\Gamma_e \times B = (B \cdot \Omega)\Gamma_e - (B \cdot \Gamma_e)\Omega + G \times B$$

Using $\Gamma_e - \frac{q}{m v_m}(\Gamma_e \times B) = G$, we can plug our expression for $\Gamma_e \times B$:

$$\Gamma_e - \frac{q}{m v_m}\left[(B \cdot \Omega)\Gamma - (B \cdot \Gamma_e)\Omega + G \times B\right]$$

Expanding the $\frac{q}{m v_m}$ term out and colecting all Γ_e terms to one side gives:

$$\Gamma_e + (\Omega \cdot \Omega)\Gamma = G - G \times \Omega + (\Omega \cdot G)\Omega$$

$$\Gamma_e(1 + \Omega^2) = G - G \times \Omega + (\Omega \cdot G)\Omega$$

$$\Gamma_e = \frac{1}{1 + \Omega^2}\left(G - G \times \Omega + (\Omega \cdot G)\Omega\right) \tag{B.2}$$

Appendix C

Theoretical Model for Vibrational Resolved Cross-Sections

Theoretical Model

Within the updated cross-section datasets for electron–deuterium molecule collisions, the vibrational levels of the D_2 molecule are resolved for vibrational excitation (VE), dissociative attachment (DA), and dissociative excitation (DE), as summarized in [14]. In this scheme, the ground electronic state is denoted as $X^1\Sigma_g^+$, while the first two excited electronic states are represented by $b^1\Sigma_u^+$ and $b^3\Sigma_u^+$, respectively. The cross sections for VE, DA, and DE were computed using the Local Complex Potential (LCP) method. This method along with the elemantary cross-sections shown in Table 4.1 are sourced from [14], and are given mathematical given by:

$$\sigma^{\mathrm{VE}}_{s,v\to s',v'}(E) = \sum_{r\in\mathcal{R}} \frac{2S_r+1}{(2S_i+1)\cdot g_2} \cdot \frac{64\pi^3 m_e^2 k'}{k} \cdot \left|\langle \chi^r_{v'} | V^r_s | \zeta^r_v \rangle\right|^2, \qquad s,s' \in \mathcal{S} \tag{C.1}$$

$$\sigma^{\mathrm{DA}}_{s,v}(E) = \sum_{r\in\mathcal{R}} \frac{2S_r+1}{(2S_i+1)\cdot g_2} \cdot \frac{g_r}{2g_s} \cdot \frac{2\pi^2 K m}{\mu k} \cdot \lim_{R\to\infty} \left|\zeta^r_{s,v}(R)\right|^2 s \in \mathcal{S} \tag{C.2}$$

$$\sigma^{\mathrm{DE}}_{s,v}(E) = \sum_{r\in\mathcal{R}} \frac{2S_r+1}{(2S_i+1)\cdot 2} \cdot \frac{g_r}{2g_s} \cdot \frac{64\pi^5 m^2}{\hbar^4} \cdot \int_{\epsilon_{\mathrm{thr}}}^{\epsilon_{\max}} d\epsilon_c \, \frac{k'}{k} \cdot \left|\left\langle \chi^{s'}_c \middle| V^{s'}_r \middle| \zeta^r_{s,v} \right\rangle\right|^2 s \in \mathcal{S} \tag{C.3}$$

These expressions provide the vibrationally and electronically resolved probabilities of scattering, attachment, and dissociation processes relevant for kinetic plasma modeling. In particular, the LCP method enables accurate treatment of resonant electron interactions with molecular D_2, which are essential for describing particle sources and energy dissipation in low-temperature hydrogenic plasmas such as those found in fusion edge regions and negative ion sources [14].

Symbol	**Definition**
$\sigma^{\mathrm{VE}}, \sigma^{\mathrm{DA}}, \sigma^{\mathrm{DE}}$	Cross sections for VE, DA, DE
E	Incident electron energy in the center-of-mass frame
α_i, α_f	Initial and final electronic states of D_2
ν_i, ν_f	Initial and final vibrational levels of D_2
$\mathcal{R}$	Set of resonant electronic states of $D_2{}^-$
$\mathcal{S}$	Set of spin states
S_i, S_r	Spin quantum numbers of D_2 and $D_2{}^-$
g_2	Statistical weight of D_2
k, k'	Wave numbers of the incoming and outgoing electron
m_e	Electron mass
μ	Reduced mass of dissociating fragments
K	Asymptotic momentum of DA dissociating fragments
R	Internuclear distance
V^r	Resonant potential for channel r
$\psi^r_{\alpha\nu}(R)$	Vibrational wavefunction in electronic state α for channel r
$\chi^r_{s'}$	Continuum final state wavefunction (DE process)
E_{th}	Dissociation threshold energy
ϵ_k	Kinetic energy of dissociation products (DE)

Bibliography

[1] G. Fubiani et al., "New J. Phys. 19, 015002", 2017.

[2] M. A. Lieberman and A. J. Lichtenberg, *Principles of Plasma Discharges and Materials Processing*, 2nd ed., John Wiley and Sons, 2005.

[3] L. Brieda, *Plasma Simulations By Example*, CreateSpace Independent Publishing Platform, 2019.

[4] D. R. Nicholson, *Introduction to Plasma Theory*, Wiley, New York, 1983.

[5] K. Miyamoto and T. Shibata, "Electrostatic and Electromagnetic Particle-In-Cell Modelling with Monte-Carlo Collision for Negative Ion Source Plasmas," in *Physics and Applications of Hydrogen Negative Ion Sources*, M. Bacal (Ed.), Springer Series on Atomic, Optical, and Plasma Physics, Vol. 124, pp. 101-138, 2023. DOI: 10.1007/978-3-031-21476-9.

[6] M. Minelli, "Particle-In-Cell Modelling of Negative Ion Sources for Fusion Applications," in *Physics and Applications of Hydrogen Negative Ion Sources*, M. Bacal (Ed.), Springer Series on Atomic, Optical, and Plasma Physics, Vol. 124, pp. 71-100, 2023. DOI: 10.1007/978-3-031-21476-9.

[7] A. George, S. Melanson, D. Potkins, M. Dehnel, N. Broderick, and H. McDonald, "Optimization of D-Ion Production in a Multicusp Ion Source," *International Particle Accelerator Conference*, Vancouver, BC, Canada, 2018. DOI: 10.18429/JACoW-IPAC2018-TUPML030.

[8] T. S. Duh, W. J. Shin, L. H. Shen, G. Ting, Y. K. Fu, and T. Kuo, "The Current Status and Future Prospects of TR 30/15 H-/D- Cyclotron Facility at INER in Taiwan," *Proceedings of the 17th International Conference on Cyclotrons and their Applications*, pp. 148, Tokyo, Japan, JACoW, October 18-22, 2004.

[9] Filament Powered Turnkey Negative Ion Source System", D-Pace Specification Sheet ISV.F040, TRIUMF-licensed, DC, volume-cusp source

[10] U. Fantz, L. Schiesko, and D. Wuenderlich, "A Comparison of Hydrogen and Deuterium Plasmas in the IPP Prototype Ion Source for Fusion," *3rd International Symposium on Negative Ions, Beams and Sources (NIBS)*, Vol. 1515, 2013. DOI: 10.1063/1.4792785.

[11] M. Dehnel, C. Hoehr, S. Melanson, A. George, N. Savard. "H-, D-, He++ Source Developments for Medical Isotope Production Cyclotrons", 2024International Topical Meeting on Nuclear Applications of Accelerators, Jefferson Lab, Norfolk, Virginia, USA, March 17-21, 2024"

[12] D. L. Shmelev, V. I. Oreshkin, and S. A. Chaikovsky, "Hybrid MHD/PIC Simulation of a Deuterium Gas Puff Z Pinch," *Journal of Physics: Conference Series*, Vol. 830(1), 012018, May 2017. DOI: 10.1088/1742-6596/830/1/012018.

[13] R. K. Janev, W. D. Langer, D. E. Post, and K. Evans, *Elementary Processes in Hydrogen-Helium Plasmas: Cross Sections and Reaction Rate Coefficients*, Springer Series on Atomic, Optical, and Plasma Physics, Vol. 4, 1987.

[14] V. Laporta, R. Agnello, G. Fubiani, I. Furno, C. Hill, D. Reiter, and F. Taccogna, "Vibrational Excitation and Dissociation of Deuterium Molecule by Electron Impact," *Plasma Physics and Controlled Fusion*, Vol. 63(8), 085006, 2021.

[15] R. Celiberto et al., "Atomic Data and Nuclear Data Tables," Vol. 77, pp. 161-213, 2001.

[16] Krishnakumar E, Denifl S, ˇCadež I, Markelj S and Mason N J

[17] Taccogna F and Minelli P 2017 New J. Phys. 19 015012

[18] Bacal M and Wada M 2020 Plasma Sources Sci. Technol. 9 033001

[19] Serianni G et al 2020 Rev. Sci. Instrum. 91 023510

[20] Furno I, Agnello R, Fantz U, Howling A, Jacquier R, Marini C, Plyushchev G, Guittienne P and Simonin A 2017 EPJ Web Conf. 157 03014

[21] Fubiani G et al 2021 in preparation